J. Fluid Mech. (2010), *vol.* 650, *pp.* 5–55. © Cambridge University Press 2010
doi:10.1017/S0022112009994022

Modulation of isotropic turbulence by particles of Taylor length-scale size

FRANCESCO LUCCI[1], ANTONINO FERRANTE[2]
AND SAID ELGHOBASHI[1]†

[1]Department of Mechanical and Aerospace Engineering, University of California, Irvine, CA 92697, USA
[2]Department of Aeronautics and Astronautics, University of Washington, Seattle, WA 98195, USA

(Received 23 June 2009; revised 13 December 2009; accepted 15 December 2009;
first published online 19 March 2010)

This study investigates the two-way coupling effects of *finite-size* solid spherical particles on decaying isotropic turbulence using direct numerical simulation with an immersed boundary method. We fully resolve all the relevant scales of turbulence around freely moving particles of the Taylor length-scale size, $1.2 \leqslant d/\lambda \leqslant 2.6$. The particle diameter and Stokes number in terms of Kolmogorov length- and time scales are $16 \leqslant d/\eta \leqslant 35$ and $38 \leqslant \tau_p/\tau_k \leqslant 178$, respectively, at the time the particles are released in the flow. The particles mass fraction range is $0.026 \leqslant \phi_m \leqslant 1.0$, corresponding to a volume fraction of $0.01 \leqslant \phi_v \leqslant 0.1$ and density ratio of $2.56 \leqslant \rho_p/\rho_f \leqslant 10$. The maximum number of dispersed particles is 6400 for $\phi_v = 0.1$. The typical particle Reynolds number is of $O(10)$. The effects of the particles on the temporal development of turbulence kinetic energy $E(t)$, its dissipation rate (t), its two-way coupling rate of change $\Psi_p(t)$ and frequency spectra $E(\omega)$ are discussed.

In contrast to particles with $d < \eta$, the effect of the particles in this study, with $d > \eta$, is that $E(t)$ is always smaller than that of the single-phase flow. In addition, $\Psi_p(t)$ is always positive for particles with $d > \eta$, whereas it can be positive or negative for particles with $d < \eta$.

1. Introduction

Simulating dispersed particles (solid particles, liquid droplets or gaseous bubbles) in a turbulent flow as *point particles* is justified if the diameter of the particle d is much smaller than the Kolmogorov length scale η and the Reynolds number of the particle $Re_p < 1$, as was demonstrated by Elghobashi & Truesdell (1992) in comparing their direct numerical simulation (DNS) results with the experimental data of Snyder & Lumley (1971) for the dispersion of solid particles in decaying isotropic turbulence (i.e. one-way coupling). The above two conditions permit using the equation of particle motion (Maxey & Riley 1983) with the Stokes drag to calculate the instantaneous particle velocity. The *point particle* approach was also used in DNS to study the effects of the particles on turbulence (two-way coupling) by Elghobashi & Truesdell (1993) and Ferrante & Elghobashi (2003). If the above two conditions, $d \ll \eta$ and $Re_p < 1$, are not satisfied, then it is not possible to derive an exact analytical equation describing the particle motion in a turbulent flow (Lumley 1978), and consequently the *point particle* approach is not justified.

---

† Email address for correspondence: selghoba@uci.edu

The only accurate approach to simulate the motion of particles whose diameter $d > \eta$ (hereinafter referred to as *finite-size* particles) in a turbulent flow is to numerically resolve the fluid motion around each individual moving particle. Few studies that resolve the flow around *freely moving* particles (or bubbles) in a turbulent flow have been recently published: Ten Cate *et al.* (2004), Lu, Fernandez & Tryggvason (2005), Zhang & Prosperetti (2005) and Uhlmann (2005). A brief description of the methods used in these four studies is given below. Ten Cate *et al.* (2004) performed fully resolved simulations of spherical particles suspended in a forced isotropic turbulence via a lattice-Boltzmann (LB) scheme. They used the LB scheme developed by Eggels & Somers (1995), in which the fluid is modelled as a number of particles, each of a dimensionless mass density n_i that propagates with discrete velocities c_i, $i = 1, M$, at discrete time steps Δt on a uniform grid (lattice) according to the lattice-Boltzmann equation:

$$n_i(x + c_i\Delta t,\ t + \Delta t) = n_i(x, t) + \Gamma_i(\boldsymbol{n}), \tag{1.1}$$

where Γ_i is the collision operator that depends on all masses, i.e. the vector $\boldsymbol{n}$, involved in the collision. The sphere surface was represented by a set of control points, placed at the sphere's surface, evenly spaced at a distance apart somewhat smaller than the grid spacing. The surface velocity was given by the sum of the translational and rotational velocity components. A body force was applied to the fluid domain such that the fluid velocity near the surface of the solid particle is equal to the velocity of the solid surface, thus satisfying the no-slip boundary condition. A spectral forcing scheme was applied to maintain the turbulent conditions at $Re_\lambda = 61$. The number of particles ranged from 773 to 3868. The volume fraction of particles ranged between 2 % and 10 %. The ratio of particle to fluid density varied between 1.15 and 1.73. A lubrication force was used to account for subgrid hydrodynamic interaction between approaching particles. The energy spectra, $E(k)$, in the wavenumber space showed that the particles generate fluid motion at length scales of the order of the particle size. This results in a strong increase in the rate of energy dissipation at these length scales and a decrease of kinetic energy at larger length scales. However, the spectra of both the turbulence energy, $E(k)$, and its dissipation rate, $\varepsilon(k)$, in figure 6 of Ten Cate *et al.* (2004), show unphysical oscillations at wavenumbers larger than those corresponding to the particle diameter. Ten Cate *et al.* (2004) stated that the effects of these oscillations on the total energy and dissipation rate are negligible. We will explain later in § 3.3.4 the details of how these oscillations are generated and describe an alternative approach to compute the energy spectra in the frequency space rather than the wavenumber space.

Lu *et al.* (2005) simulated the flow around 16 deformable bubbles freely moving in a 'minimum turbulent channel'. They solved the Navier–Stokes equations by a second-order accurate projection method using centred differences on a fixed staggered grid. The bubble surface (*front*) was explicitly marked by connected marker points that form an unstructured triangular grid. The front points were advected by the flow velocity, interpolated from the fixed grid. The front was used to update the density and viscosity at each grid point and to find the surface tension. As the front deforms, surface markers were dynamically added and deleted. The surface tension was represented by a distribution of singularities (δ functions) located at the front. To transfer the front singularities to the fixed grid, the δ functions were approximated by smoother functions with a compact support on the fixed grid.

Zhang & Prosperetti (2005) developed a numerical method (named Physalis) to resolve the flow around spherical particles freely moving in an incompressible flow.

The basic idea of Physalis is that, due to the no-slip condition, in the reference frame of each particle, the fluid velocity near the particle boundary is very small so that the Stokes equations constitute an excellent approximation to the full Navier–Stokes equations. The general analytical solution of the Stokes equations can then be used to 'transfer' the no-slip condition from the particle surface to the adjacent grid nodes. In this way, the geometric complexity arising from the irregular relation between the particle boundary and the underlying mesh is avoided and fast solvers can be used. The method has been validated by a detailed comparison with spectral solutions for the flow past a sphere at Reynolds numbers of 50 and 100. Zhang & Prosperetti (2005) applied their method to a decaying isotropic turbulence containing 100 spherical particles, randomly positioned. The cubical domain consisted of 64^3 mesh points and the initial $Re_\lambda = 29$. The ratio of particle to fluid density is $\rho_p/\rho_f = 1.02$, where ρ_f is the density of the carrier fluid. The volume fraction of the particles is $\phi_v = 0.1$. The particle diameter is $d/\eta_0 = 8.32$, where η_0 was the initial Kolmogorov length scale. The Physalis method is quite accurate because it uses the analytical solution of the Stokes equations in the vicinity of the spherical particle surface and thus the no-slip condition is satisfied exactly at the surface. However, Physalis is limited to non-deformable spherical particles. Simulating the deformation of the particle surface would be necessary in cases of particle or droplet combustion or the motion of large bubbles. Uhlmann (2005) used the *immersed boundary* (IB) method, which was originally developed by Peskin (1972, 2002), to solve the incompressible continuity and Navier–Stokes equations for flows around flexible membranes, e.g. the flow in the human heart. The IB formulation (Peskin 2002) involves both Eulerian and Lagrangian variables linked by the Dirac delta function. Spatial discretization of the governing fluid equations is based on a fixed Cartesian mesh for the Eulerian variables and a moving curvilinear mesh for the Lagrangian variables. The two types of variables are linked by interaction equations that involve a smoothed approximation to the Dirac delta function. Eulerian/Lagrangian identities govern the transfer of data from one mesh to the other. For example, in the case of a freely moving solid particle, a singular force is applied at prescribed Lagrangian points (distributed evenly on the moving sphere surface; figure 1) to the Navier–Stokes equations via a delta function. The regularized three-point delta function proposed by Roma, Peskin & Berger (1999) is essential to the efficiency of this method. A schematic of the Eulerian/Lagrangian mesh details and δ function is given in figure 2.

Uhlmann (2005) improved the IB method by minimizing the numerical oscillations resulting from the interaction forces between the fluid and the immersed solid body. He also presented simulations of the sedimentation of 2000 identical spherical particles under the effect of gravity, with a terminal Reynolds number ≈ 400, in a periodic box. More recently, Uhlmann (2008) applied the IB method to the two-way interactions between 4096 spherical particles and a fully developed turbulent channel flow using a uniform Cartesian mesh with $2048 \times 513 \times 1024$ grid points. The volume fraction of the particles is 4.2×10^{-3} and the particle diameter is about 10 viscous wall units. At present, the DNS study of Uhlmann (2008) has the largest number of fully resolved moving particles in a turbulent flow.

We adopt a modified version of the IB method of Uhlmann (2005) to study the two-way coupling effects of finite-size particles in a decaying isotropic turbulence. We fully resolve all the relevant scales of turbulence around freely moving spherical particles of the Taylor length-scale size, $1.2 \leqslant d/\lambda \leqslant 2.6$. The particle diameter and Stokes number in terms of Kolmogorov length- and time-scales are $16 \leqslant d/\eta \leqslant 35$ and

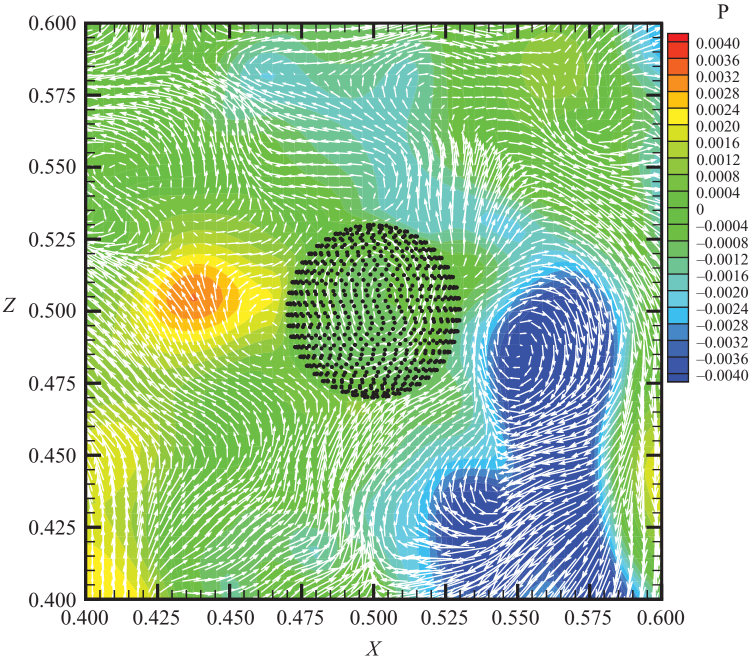

FIGURE 1. Pressure distribution and velocity vectors around a spherical solid particle in isotropic turbulence. Only a small region of the middle plane of the computational domain is shown. The black dots represent the Lagrangian points on the sphere surface where the two-way coupling force is imparted on the surrounding fluid.

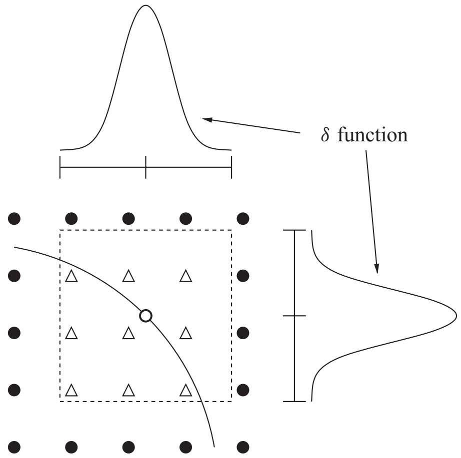

FIGURE 2. Eulerian grid points (triangles) influenced by the force at the Lagrangian grid point (white circle) of the particle spherical surface (black line). Three-dimensional, three-point δ function by Roma *et al.* (1999).

$38 \leqslant \tau_p/\tau_k \leqslant 178$, respectively, at the time the particles are released in the flow. The particles mass fraction range is $0.026 \leqslant \phi_m \leqslant 1.0$, corresponding to a volume fraction of $0.01 \leqslant \phi_v \leqslant 0.1$ and density ratio of $2.56 \leqslant \rho_p/\rho_f \leqslant 10$. The maximum number of dispersed particles is 6400 for $\phi_v = 0.1$.

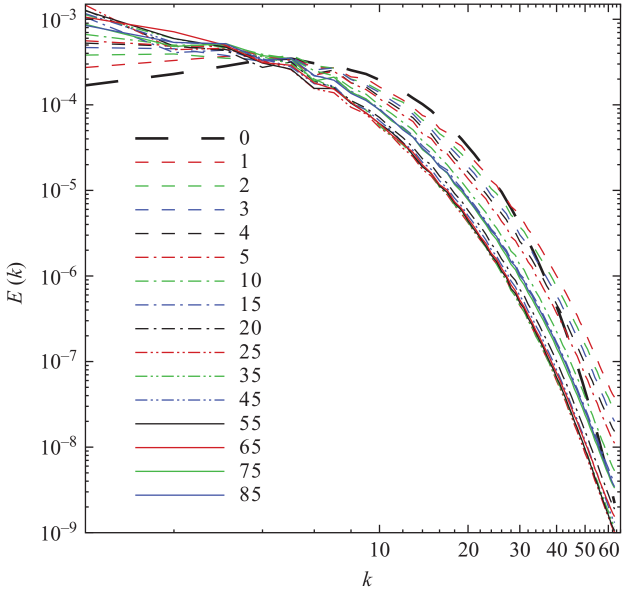

FIGURE 3. Temporal development of the energy spectrum, $E(k, t)$, as a result of forcing in the physical space to produce stationary turbulence, $\mathrm{d}E/\mathrm{d}t = 0$. The numbers next to the line symbols indicate dimensionless time.

It should be mentioned that other studies have used forced isotropic turbulence to maintain a *statistically stationary turbulence* at higher values of Reynolds number, Re_λ, for a given grid resolution, than those in decaying turbulence. Forcing isotropic turbulence, whether spectrally at the small wave numbers or in the physical space, is an appropriate approach to study the small-scale motion (large wavenumbers) in single-phase flows or the dispersion of particles (one-way coupling) in particle-laden turbulent flows. However, it is certainly incorrect to use any forcing to study the two-way coupling effects of dispersed particles on turbulence for the following reasons:

(*a*) If forcing is performed in the spectral space by adding energy at the smallest wavenumber, the amplitude of the temporal variation of the turbulence kinetic energy (TKE), $E(t)$, in the forced simulations of single-phase isotropic turbulence can be as large as 50 % of the time-mean value of $E(t)$ (see figure 6 of Rosales & Meneveau 2005). This large fluctuation of $E(t)$ due to forcing is of the order of the modulation of $E(t)$ by the two-way coupling effects of the dispersed particles, and thus it is impossible to accurately quantify the true effects of the two-way coupling.

(*b*) If forcing is performed in the physical space, for example, according to

$$\mathrm{D}u_i/\mathrm{D}t = \cdots + \frac{u_i\ \varepsilon(t)}{2E(t)},$$

which is equivalent to

$$\mathrm{D}E/\mathrm{D}t = -\varepsilon(t) + \frac{\langle u_i^2\rangle\ \varepsilon(t)}{2E(t)} = -\varepsilon(t)\ + \varepsilon(t) = 0,$$

the turbulence energy $E(t)$ becomes invariant, where $\varepsilon(t)$ is the dissipation rate of $E(t)$. However, this stationarity of $E(t)$ is achieved by continually modifying the spectrum $E(k, t)$ at all wavenumbers to maintain $\int E(k)\ \mathrm{d}k = constant$ as shown in figure 3.

It is seen that as time increases, $E(k)$ is reduced at medium/large wavenumbers, whereas $E(k)$ is increased at small wavenumbers. This redistribution of $E(k)$ opposes the action of the particles as discussed below.

(*c*) Although the *direct* interaction of small particles ($d < \eta$) with turbulence *starts* at length scales of the order of particle size, i.e. large wavenumbers, the triadic interactions (Elghobashi & Truesdell 1993; Ferrante & Elghobashi 2003) between these wave numbers and the small wavenumbers (large sales) are directly affected by *any* forcing mechanism, whether spectrally at the small wavenumbers or physically over all wavenumbers. The modification of the spectral transfer of energy, $T(k)$, at the small wavenumbers by the particles has been clearly demonstrated (Elghobashi & Truesdell 1993; Ferrante & Elghobashi 2003). Thus, no clear distinction can be made between the effects of the two opposing mechanisms: the *natural reduction* of $E(k)$ at small wavenumbers by the particles, and the *artificial supply* of $E(k)$ at the same wavenumbers as shown in figure 3.

Section 2 describes the governing equations and the numerical method. The DNS results are discussed in § 3. The conclusions are presented in § 4.

2. Mathematical description

2.1. *Governing equations*

The governing equations for the incompressible isotropic turbulent flow are the Navier–Stokes equations

$$\frac{\partial u_i}{\partial t} + \frac{\partial (u_i u_j)}{\partial x_j} = -\frac{\partial p}{\partial x_i} + \nu \frac{\partial^2 u_i}{\partial x_j \partial x_j} + f_i, \tag{2.1}$$

and the continuity equation

$$\frac{\partial u_i}{\partial x_i} = 0, \tag{2.2}$$

where $i = 1, 2, 3$ for the three coordinate directions x_1, x_2 and x_3. Here f_i is the net force, per unit mass of fluid, in the x_i direction at the Eulerian mesh points that are directly affected by the particle force through the three-point δ function (figure 2). Note that (2.1) and (2.2) are written in non-dimensional form, and throughout the paper all variables are dimensionless except those with superscript tilde ($\tilde{}$).

2.2. *Numerical method*

Our DNS method solves the unsteady three-dimensional Navier–Stokes and continuity equations ((2.1) and (2.2)) throughout the whole computational domain $\mathscr{D}$, *including the interior of the dispersed particles.* These governing equations are discretized in space in an Eularian framework using a second-order finite-difference scheme on a uniform staggered mesh of $(256)^3$ grid points. This grid allows an initial microscale Reynolds number $Re_{\lambda 0} = 75$. Time integration was performed via the Adams–Bashforth scheme with a time step $\Delta t = \Delta x/2$, where Δx is the grid spacing. The simulations were stopped after 10 240 time steps at non-dimensional time $t = 20$. Pressure was treated implicitly and was obtained by solving the Poisson equation in finite-difference form using a combination of a two-dimensional fast Fourier transform (FFT) in the $x_1 x_2$ plane, and Gauss elimination in the x_3 direction. Periodic boundary conditions were imposed in the three directions. The particles were released with a random distribution in the computational domain at time $t = 1$, when the skewness of the velocity derivative S_u has reached the value −0.50, indicating

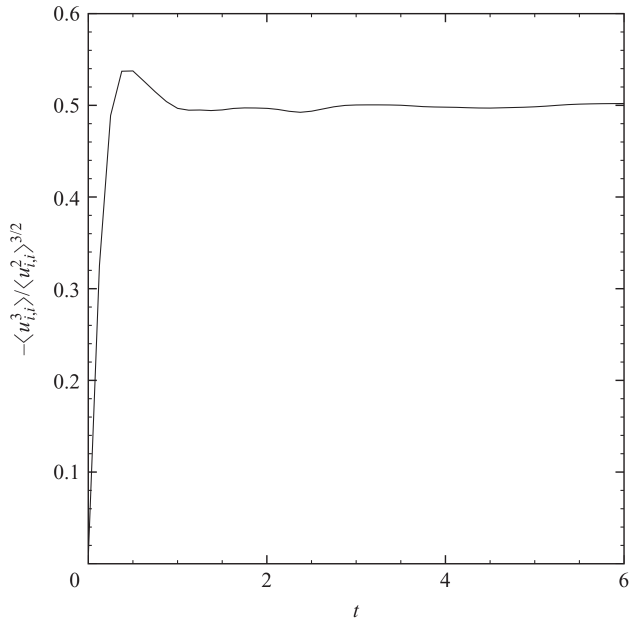

FIGURE 4. Temporal development of the skewness, S_u, of the velocity derivative in the DNS of decaying isotropic turbulence.

an established nonlinear transfer of turbulence kinetic energy across the spectrum (figure 4). We have also computed the skewness, $S(r,t)$, of the velocity increments, using the third-order structure function, $D_{LLL}(r,t) = \langle [u_1(x_1 + \boldsymbol{e}_1 r, t) - u_1(x_1, t)]^3 \rangle$, and second-order structure function, $D_{LL}(r,t) = \langle [u_1(x_1 + \boldsymbol{e}_1 r, t) - u_1(x_1, t)]^2 \rangle$, for single-phase isotropic turbulence during the time period $t = 0$ to $t = 6$ according to

$$S(r,t) = D_{LLL}(r,t)/D_{LL}(r,t)^{3/2}, \tag{2.3}$$

where $r \approx$ particle diameter $d = 1.2\lambda = 16.4\eta$. Figure 5 shows that $-S(d,t)$ increases from zero to a peak of about 0.33 at $t = 0.5$, then it remains fairly stationary at an average value of about 0.3 until $t = 6$ (about two eddy turnover times), indicating the non-Gaussian nonlinearity of the velocity field at the scales of particle size. In the particle-laden cases, the particles are released into the flow at $t = 1$. It should be noted that for isotropic turbulence at a much higher Re_λ than in our present flow, the Kolmogorov theory predicts for the inertial range, a value of $S(r) = -(4/5)/(2.1)^{3/2} \approx -0.26$ whose magnitude is slightly lower than ours.

The time $t = 1$ will be referred to hereinafter as the ‘injection time’, t_{inj}. The initial velocity at t_{inj} of each particle was set equal to the instantaneous fluid velocity at the particle centre. The linear and angular velocities of the particle were computed via (2.19) and (2.20), and were used to calculate the instantaneous particle trajectories. The motion of the particles was fully coupled to that of the fluid. This coupling method was developed by Ferrante & Elghobashi (2007) and is a modified version of the IB method proposed by Uhlmann (2005). The details of the numerical approach is given in the following subsections. The main differences between the current method and that of Uhlmann (2005) are as follows:

(*a*) Our time integration is performed using the second-order Adams–Bashforth scheme (2.6), instead of a third-order Runge–Kutta scheme used by Uhlmann (2005);

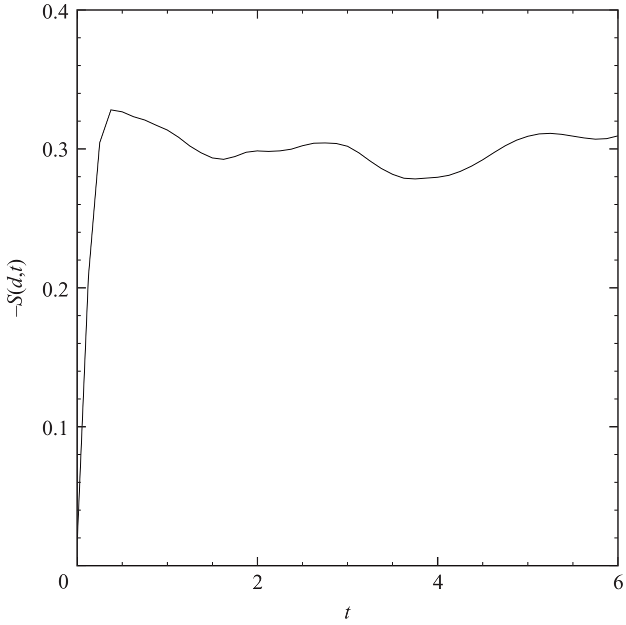

FIGURE 5. Skewness, $-S(d,t)$, of the velocity increments in single-phase isotropic turbulence at scales equal to the particle diameter.

(*b*) The pressure-gradient term of the time level n is not included in (2.6), in contrast to (12*a*) of Uhlmann (2005);

(*c*) The two-way coupling force is directly applied to the velocity field according to (2.16) without solving the Helmholtz equation, in contrast to (12*e*) of Uhlmann (2005);

(*d*) At each time step, only one Poisson equation (2.17) for the pressure is solved, in contrast to the method of Uhlmann (2005), who solved one Poisson equation and one vectorial (three scalar) Helmholtz equation for each of the three Runge–Kutta steps, (12*e*) and (12*f*).

2.2.1. *DNS of the carrier flow*

The fluid acceleration, RU_i, due to the inertia and viscous forces, is defined as

$$RU_i = -\partial_j(u_i u_j) + \nu\partial_j\partial_j u_i. \tag{2.4}$$

Equation (2.1) is recast in a compact form as

$$\partial_t u_i = -\partial_i p + RU_i + f_i. \tag{2.5}$$

The following five steps constitute the numerical algorithm of the flow solver:

(*a*) Time integration of (2.5), without the pressure gradient and force f_i, is performed using the Adams–Bashforth scheme:

$$\frac{u_i^* - u_i^n}{\Delta t} = \frac{3}{2}\,RU_i^n - \frac{1}{2}\,RU_i^{n-1}, \tag{2.6}$$

where u_i^* is an approximate value of u_i^{n+1} before applying the forcing (2.16) and the pressure correction (2.18).

(*b*) The instantaneous force components f_i in the x_i directions are computed via the next three sub-steps:

$$U_i^*\left(\boldsymbol{X}_l^{(m)}\right) = \sum_{\boldsymbol{x}\in\mathscr{D}} u_i^*(\boldsymbol{x})\,\delta_h\left(\boldsymbol{x}-\boldsymbol{X}_l^{(m)}\right) h^3, \quad \forall\, l, m, \tag{2.7}$$

$$F_i\left(\boldsymbol{X}_l^{(m)}\right) = \frac{U_i^{(d)}\left(\boldsymbol{X}_l^{(m)}\right) - U_i^*\left(\boldsymbol{X}_l^{(m)}\right)}{\Delta t}, \quad \forall\, l, m, \tag{2.8}$$

$$f_i(\boldsymbol{x}) = \sum_{m=1}^{N_p}\sum_{l=1}^{N_L} F_i\left(\boldsymbol{X}_l^{(m)}\right)\delta_h\left(\boldsymbol{x}-\boldsymbol{X}_l^{(m)}\right)\Delta V_l^{(m)}, \tag{2.9}$$

where the lower-case letters denote quantities computed at the Eulerian mesh points $\boldsymbol{x}$, and the upper-case letters denote quantities computed at the Lagrangian force points $\boldsymbol{X}_l^{(m)}$ with $1 \leqslant m \leqslant N_p$ and $1 \leqslant l \leqslant N_L$, where N_p is the number of particles tracked and N_L is the number of Lagrangian force points distributed uniformly over the surface of each particle (figure 1). The uniform distribution of the Lagrangian points on the spherical surface of the particles was achieved by using the explicit spiral set proposed by Saff & Kuijlaars (1997). The spherical coordinates $(\theta_k, \phi_k, d/2)$ of the Lagrangian points are defined as

$$\theta_k = \arccos(c_k), \quad c_k = -1 + \frac{2(k-1)}{(N_L-1)}, \quad 1 \leqslant k \leqslant N_L, \tag{2.10}$$

$$\phi_1 = \phi_{N_L} = 0, \quad \phi_k = \left(\phi_{k-1} + \frac{3.6}{\sqrt{N_L}}\frac{1}{\sqrt{1-c_k^2}}\right), \quad 1 < k < N_L, \tag{2.11}$$

where h is the width of the uniform Eulerian mesh, and δ_h represents the three-dimensional regularized three-point delta function proposed by Roma *et al.* (1999):

$$\delta_h\left(\boldsymbol{x}-\boldsymbol{X}_l^{(m)}\right) = \frac{1}{h^3}\delta(r_1)\delta(r_2)\delta(r_3), \tag{2.12}$$

where $r_i = (x_i - (X_l^m)_i)/h$ and

$$\delta(r) = \begin{cases} \frac{1}{3}\left(1+\sqrt{1-3r^2}\right), & \text{if } |r| \leqslant 0.5, \\ \frac{1}{6}\left(5-3|r|-\sqrt{1-3(1-|r|)^2}\right), & \text{if } 0.5 \leqslant |r| \leqslant 1.5, \\ 0, & \text{if } |r| \geqslant 1.5, \end{cases} \tag{2.13}$$

for $r = r_1$, r_2 or r_3. Note that $\Delta V_l^{(m)}$ is the volume associated with each force point l of the mth particle:

$$\Delta V_l^{(m)} = \frac{\pi h}{3N_L}\left(12(d/2)^2 + h^2\right). \tag{2.14}$$

The union of all $\Delta V_l^{(m)}$ volumes for the mth particle forms a thin shell of thickness h around the particle. The desired velocity, $U_i^{(d)}$ in (2.8), at the interface between carrier fluid and particle is computed according to the rigid-body motion of the particle surface as

$$\boldsymbol{U}^{(d)}\left(\boldsymbol{X}_l^{(m)}\right) = \boldsymbol{v}^{(m)} + \boldsymbol{\omega}_p^{(m)} \times \left(\boldsymbol{X}_l^{(m)} - \boldsymbol{x}_p^{(m)}\right), \tag{2.15}$$

where $\boldsymbol{v}^{(m)}$, $\boldsymbol{\omega}_p^{(m)}$ and $\boldsymbol{x}_p^{(m)}$ are the translational velocity, rotational velocity and centre coordinates, respectively, of the mth particle. The algorithm used to compute these quantities is described in the following subsection.

(*c*) The force imparted by the particle is applied by updating u_i^* as

$$\hat{u}_i^* = u_i^* + \Delta t\, f_i. \tag{2.16}$$

(*d*) The pressure is computed by solving the Poisson equation:

$$\nabla^2 p^{n+1/2} = \frac{\partial_j \hat{u}_j^*}{\Delta t}. \tag{2.17}$$

(*e*) The fluid velocity is corrected with the pressure gradient according to

$$u_i^{n+1} = \hat{u}_i^* - \Delta t\, \partial_i p^{n+1/2}. \tag{2.18}$$

The projection method ((2.6), (2.16), (2.17) and (2.18)) is second-order accurate in space and time for the velocity u_i, but first-order accurate in time for the pressure, p (see Brown, Cortez & Minion 2001). Since the computed pressure is used exclusively to impose the condition of divergence-free velocity, the presented results are not affected by the lower-order pressure.

2.2.2. *DNS of particle motion*

The equations of conservation of linear and angular momenta for a solid particle moving in an incompressible fluid, derived in the Appendix, are

$$\left(\rho_p^{(m)} - \rho_f\right) V_p^{(m)} \dot{\boldsymbol{u}}_p^{(m)} = -\rho_f \sum_{l=1}^{N_L} \boldsymbol{F}\left(\boldsymbol{X}_l^{(m)}\right) \Delta V_l^{(m)} + \left(\rho_p^{(m)} - \rho_f\right) V_p^{(m)} \boldsymbol{g} + \boldsymbol{F}_R^{(m)}, \tag{2.19}$$

$$I_p^{(m)} \dot{\boldsymbol{\omega}}_p^{(m)} = -\rho_f \sum_{l=1}^{N_L} \left(\boldsymbol{X}_l^{(m)} - \boldsymbol{x}_p^{(m)}\right) \times \boldsymbol{F}\left(\boldsymbol{X}_l^{(m)}\right) \Delta V_l^{(m)} + \rho_f \frac{\mathrm{d}}{\mathrm{d}t} \int\!\!\int\!\!\int_{\mathscr{V}^{(m)}} \left[\left(\boldsymbol{x} - \boldsymbol{x}_p^{(m)}\right) \times \boldsymbol{u}\right] \mathrm{d}\boldsymbol{x}, \tag{2.20}$$

where $V_p^{(m)}$, $I_p^{(m)}$ and $\rho_p^{(m)}$ are the volume, moment of inertia and density of the mth particle, respectively, ρ_f is the density of the carrier fluid and $\boldsymbol{g}$ is the gravitational acceleration.

In order to avoid the overlapping of particles (or penetration into each other), we included the repulsive force $\boldsymbol{F}_R^{(m)}$ on the right-hand side of (2.19). This force is computed as the sum of the *short-range* repulsive forces between pairs of particles whose centres are at a distance smaller than $d + d_R$, where d is the particle diameter (the same for all particles) and d_R is a prescribed distance (force range):

$$\boldsymbol{F}_R^{(m)} = \sum_{\substack{j=1,\\ j\neq m,}}^{N_p} \boldsymbol{F}_R^{(m,j)}, \tag{2.21}$$

The repulsive force between particles m and j, $\boldsymbol{F}_R^{(m,j)}$, is computed according to Glowinski *et al.* (2001) as

$$\boldsymbol{F}_R^{(m,j)} = \begin{cases} 0, & \text{if } d^{(m,j)} \geqslant d + d_R, \\ \dfrac{1}{\epsilon_R}\left(\dfrac{d + d_R - d^{(m,j)}}{d_R}\right)^2 \left(\dfrac{\boldsymbol{x}_m - \boldsymbol{x}_j}{d^{(m,j)}}\right), & \text{if } d^{(m,j)} < d + d_R, \end{cases} \tag{2.22}$$

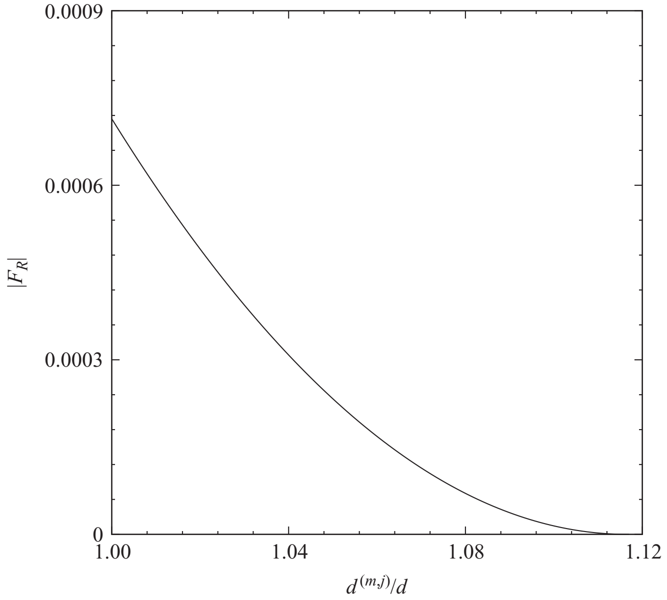

FIGURE 6. Repulsive force magnitude (dimensionless) versus the normalized distance between the particles centres, $d^{(m,j)}/d$ in case H.

where $d^{(m,j)}$ is the distance between the centres of particles m and j, and ϵ_R is a *stiffness* parameter computed for each case as

$$\epsilon_R = \frac{\rho_{p,H} V_{p,H}^{(m)}}{\rho_p V_p^{(m)}} \epsilon_{R,H}, \tag{2.23}$$

where subscript H refers to case H (table 3). In our simulations, the two parameters d_R and $\epsilon_{R,H}$ were prescribed as $d_R = 2\Delta x$ and $\epsilon_{R,H} = 1.4 \times 10^3$. Figure 6 shows the variation of the magnitude of the repulsive force with the normalized distance between the particles centres, $d^{(m,j)}/d$. These values of d_R and $\epsilon_{R,H}$ were chosen to first minimize the number of particle–particle overlappings, and then minimize the number of particles for which $\boldsymbol{F}_R^{(m)}$ is non-zero. For example, in case H ($\phi_v = 0.1$), the number of particle–particle overlappings was reduced from about 2×10^2 at $t = 5$ for the simulation without repulsive force to zero for the whole simulation with repulsive force. Also, the repulsive force is non-zero only for about 4 % of the total number of particles. Furthermore, it should be noted that the temporal development of the turbulence kinetic energy does not change significantly whether or not the repulsive force, with the above values of d_R and ϵ_R, is included.

3. Results and discussion

3.1. *Settling sphere validation*

In order to validate the numerical method presented in § 2.2, we have simulated the motion of a settling spherical particle in a quiescent fluid. The physical parameters in our simulation are set identical to those of the experiments conducted by Mordant & Pinton (2000). In the experiment, a steel spherical particle ($\tilde{\rho}_f = 7710$ kg m^{-3}) of diameter $\tilde{d} = 0.8$ mm was released from rest in quiescent water ($\tilde{\nu} = 0.9 \times 10^{-6}$ m^2 s^{-1}, $\tilde{\rho}_f = 1000$ kg m^{-3}). Under the effect of gravity the sphere reaches its settling velocity

	$\tilde{V}_t$ (m s^{-1})	$\tilde{\tau}_{95}$ (s)
Present simulation	0.309	106.4×10^{-3}
Experiments by Mordant & Pinton (2000)	0.316	108×10^{-3}

TABLE 1. Settling particle velocity $\tilde{V}_t$ and particle response time $\tilde{\tau}_{95}$. Comparison of the present DNS with the experiment of Mordant & Pinton (2000).

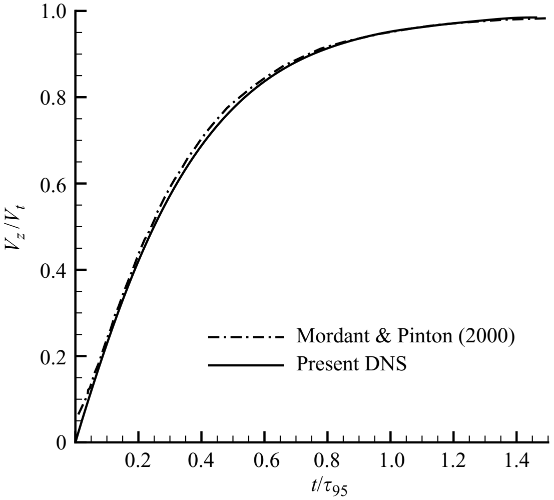

FIGURE 7. Temporal development of normalized vertical velocity V_z/V_t for a single settling sphere. Comparison of the present DNS with the experiment of Mordant & Pinton (2000).

$\tilde{V}_t = 0.316\,\mathrm{m\,s^{-1}}$. The Reynolds number based on particle settling velocity and particle diameter is $Re_p = 280$.

For this test case the domain is a parallelepiped with dimensionless sides $L_x = 1$, $L_y = 1$ and $L_z = 10$. Gravity is oriented in the z direction. The computational mesh is equispaced in the three directions. The particle has a dimensionless diameter $d = 0.08$. The particle/fluid density ratio is $\rho_p/\rho_f = 7.71$, and fluid dimensionless kinematic viscosity is $\nu = 2.85 \times 10^{-4}$. Periodic boundary conditions are applied in all three directions. Because of the imposed periodicity in the z direction, the wake of the particle could enter from the bottom of the computational domain and interact directly with the surface of the falling particle. However, the domain is sufficiently long in the vertical direction ($L_z = 62.5\,d$) and the simulation is stopped when the particle has moved for a length of $25\,d$ such that periodicity in z has negligible effects on the particle motion.

Figure 7 shows the temporal development of the vertical velocity $V_z(t)$ normalized by the experimental settling velocity. This figure shows that our numerical solution is in excellent agreement with the experimental velocity measured by Mordant & Pinton (2000). The computed final velocity and particle response time $\tilde{\tau}_{95}$ (defined as the time for the particle to reach 95 % of its settling velocity) differ from the experimental results for less than 1.5 % (table 1).

t	u_{urms}	ε	ℓ	λ	η	Re_ℓ	Re_λ	ℓ/η	τ_ℓ	τ_λ	τ_k
0.0	0.0503	7.4×10^{-4}	0.0684	0.0345	0.00202	150	75	33.8	1.36	0.68	0.177
1.0	0.0436	9.8×10^{-4}	0.0685	0.0259	0.00188	129	49	36.4	1.57	0.59	0.154
5.0	0.0233	2.0×10^{-4}	0.0891	0.0305	0.00280	90	31	31.9	3.83	1.31	0.338
20.0	0.0097	9.2×10^{-6}	0.1407	0.0594	0.00608	58	25	23.1	14.6	6.15	1.588

TABLE 2. Flow parameters (dimensionless) at initial time ($t = 0$), injection time ($t = 1$), and only for case A at time $t = 5$ and 20.

3.2. *Turbulence and particle properties*

The initial velocity field was generated by prescribing the turbulence kinetic energy spectrum $E(k)$ and ensuring that the initial random velocity field is isotropic, divergence-free with respect to the discretized form of the continuity equation, and that the velocity cross-correlation spectra, $R_{ij}(k)$, satisfy the realizability constraints (Schumann 1977). The initial energy spectrum at time $t = 0$ was prescribed via

$$E(k) = \left(\frac{3u_0^2}{2}\right)\left(\frac{k}{2\pi k_p^2}\right)\exp\left(-\frac{k}{k_p}\right), \tag{3.1}$$

where k is the wavenumber, k_p is the wavenumber of peak energy, and u_0 is the initial dimensionless root-mean-square (r.m.s.) velocity. In this paper, the wavenumbers are normalized by the smallest non-zero wave number, $k_{min} = 2\pi/L$, where L is the length of the computational domain ($L = 1$). Prescribing the values of k_p and u_0 determines $E(k)$ according to (3.1). The dimensionless kinematic viscosity, ν, was computed from the prescribed initial microscale Reynolds number, $Re_{\lambda 0}$, and the computed initial energy dissipation rate, $\varepsilon(0)$. The values of the dimensionless parameters at time $t = 0$ were $k_p = 4$, $u_0 = 0.0503$, $Re_{\lambda 0} = 75$, $\varepsilon_0 = 7.4 \times 10^{-4}$ and $\nu = 2.31 \times 10^{-5}$. Table 2 shows the dimensionless flow parameters at different times t for the particle-free flow (case A): l and τ_l are the integral length- and time scales; Re_l is the Reynolds number based on l; λ is the Taylor microscale; η and τ_k are the Kolmogorov length- and time scales. The values of the reference length and time scales used in normalizing the above quantities were $\tilde{L}_{ref} = 10^{-2}$ m and $\tilde{t}_{ref} = 2.33 \times 10^{-3}$ s, which together with the dimensionless viscosity ν produce the appropriate value of dimensional kinematic viscosity of the fluid (liquid water at STP) $\tilde{\nu} = 10^{-6}\,\mathrm{m^2\,s^{-1}}$. The accuracy of the computations of the single-phase flow has been verified via comparison with the well-known properties of decaying isotropic turbulence, e.g. the asymptotic value of the skewness of the velocity derivative, the decay rate of TKE, and spectra of TKE and its dissipation rate. In addition, the smallest scales of turbulence are well resolved as indicated by $\eta\, k_{max} \geqslant 1$ at all times, where $k_{max} = 2\pi N/2$ is the maximum resolved wavenumber and $N = 256$ is the number of grid points in each direction in our computational grid.

We studied seven cases (B–H) of particle-laden isotropic turbulence to explain how finite-size particles modify the decay rate of turbulence in zero gravity. The flow parameters are shown in table 2, and the particle properties are shown in table 3.

Case A represents the particle-free decaying isotropic turbulence. The effects of varying the particles volume fraction, ϕ_v, particle-to-fluid density ratio (or mass fraction, ϕ_m), and particle diameter are studied in the three sets BCD, DEF and DGH, respectively, while keeping constant the remaining two of the above three parameters. In cases B, C and D, the volume fraction increases from 0.01 to 0.1 by

Case	d	ρ_p/ρ_f	N_p	τ_p	τ_p/τ_k	d/η	d/λ	ϕ_v	ϕ_m
A	–	–	0	–	–	–	–	0	0
B	0.031	2.56	640	5.865	38.3	16.4	1.2	0.01	0.026
C	0.031	2.56	3200	5.865	38.3	16.4	1.2	0.05	0.128
D	0.031	2.56	6400	5.865	38.3	16.4	1.2	0.10	0.256
E	0.031	5.00	6400	11.46	74.5	16.4	1.2	0.10	0.500
F	0.031	10.0	6400	22.91	149	16.4	1.2	0.10	1.000
G	0.043	2.56	2304	11.43	74.3	22.9	1.7	0.10	0.256
H	0.067	2.56	640	27.40	178	35.4	2.6	0.10	0.256

Table 3. Particle properties (dimensionless) at injection time ($t = 1$).

increasing the number of particles. In cases D, E and F, the mass fraction increases from 0.256 to 1.0 by increasing the particle-to-fluid density ratio from 2.56 (e.g. glass particles in liquid water) to 10 (e.g. fuel droplets in a Diesel engine combustor). In cases D, G and H, the particle diameter is increased from 16.4η (or 1.2λ) to 35.4η (or 2.6λ), where η and λ are the Kolmogorov and Taylor length scales of turbulence, respectively, at the time of particle injection ($t = 1$). The number of Lagrangian points that define the surface of each spherical particle is $N_L = 198$ in cases B to F, $N_L = 381$ in case G, and $N_L = 925$ in case H. There are eight Eulerian grid points per diameter for cases B to F, 11 in case G and 17 in case H.

Figure 1 shows the pressure distribution and velocity vectors around a typical spherical solid particle in isotropic turbulence. The black dots represent the Lagrangian points on the sphere surface where the two-way coupling force is imparted on the surrounding fluid. We should point out that the average error $\left\langle |\boldsymbol{U}^{n+1} - \boldsymbol{U}^{(d)}|/|\boldsymbol{U}^{(d)}|\right\rangle$, i.e. the ensemble-averaged normalized difference between the desired velocity, $\boldsymbol{U}^{(d)}(\boldsymbol{X}_l^{(m)})$ defined in (2.15), and the interpolated fluid velocity at the Lagrangian points, $\boldsymbol{X}_l^{(m)}$,

$$U_i^{n+1}\left(\boldsymbol{X}_l^{(m)}\right) = \sum_{\boldsymbol{x} \in \mathscr{D}} u_i^{n+1}(\boldsymbol{x})\, \delta_h\left(\boldsymbol{x} - \boldsymbol{X}_l^{(m)}\right) h^3, \tag{3.2}$$

is about 2 %. The ensemble averaging is performed over all Lagrangian points of all particles, $N_L N_p$. That difference should be identically zero in order to satisfy the no-slip condition (at the particle surface) in a reference frame moving with the particle. In this study, the particles translate and rotate freely in the turbulent flow and, thus, the standard definition of particle Reynolds number $Re_p = |\boldsymbol{v} - \boldsymbol{u}_\infty| d/\nu$ cannot be used because the free-stream fluid velocity $\boldsymbol{u}_\infty$ cannot be uniquely defined due to the disturbances caused by the particle and its neighbouring particles. Therefore, we define the particle Reynolds number as $Re_{p1} = |\boldsymbol{v}| d/\nu$. Our results show that, at $t = 2.0$, Re_{p1} averaged over all particles, is about 65, for the light particles (case D), and 75, for the heavier particles (case F). An alternative evaluation of the Reynolds number is here proposed by computing the velocity difference between the particle translational velocity, $\boldsymbol{v}$, and the fluid velocity, $\boldsymbol{u}_d$, at a distance $d \simeq \lambda$ from the particle surface along the $\boldsymbol{v}$ direction (figure 8), and averaged over a spherical shell with solid angle $\Theta = 2\pi[1 - \cos(\pi/4)] = 1.84$ steradian, $\overline{\boldsymbol{u}}_d$. With this definition, $Re_{p2} = |\boldsymbol{v} - \overline{\boldsymbol{u}}_d| d/\nu$ is about 80 and 90 for the light particle (case D) and heavier particle (case F), respectively (figure 26). The velocity $\boldsymbol{u}(r)$ of figures 26 and 27 is computed as follows:

(a) for each Eulerian point, $\boldsymbol{x}$, of the computational domain, find the closest particle;

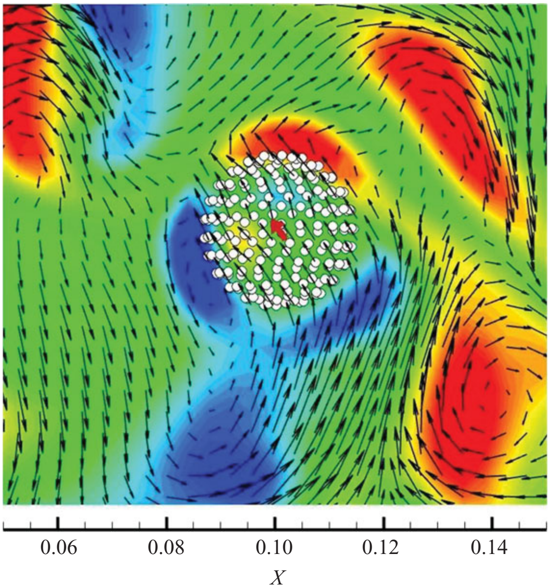

FIGURE 8. Isocontours of the vorticity normal to the plane and velocity vectors around a spherical solid particle in isotropic turbulence, the white dots represent the Lagrangian points on the sphere and the red arrow is the particle velocity vector.

(*b*) compute the distance from the closest particle surface, r;

(*c*) include the fluid velocity $\boldsymbol{u}(\boldsymbol{x})$ in the statistics of $\boldsymbol{u}(r)$ *front* region of the particle if $(\boldsymbol{x}-\boldsymbol{x}_p)\cdot\boldsymbol{v}>0$, or *back* region if $(\boldsymbol{x}-\boldsymbol{x}_p)\cdot\boldsymbol{v}<0$.

Note that throughout the text, we denote *the flow sub-domain downstream the particle trajectory* as *front* of the particle and *the flow sub-domain upstream the particle trajectory* as *back* of the particle.

In order to compute the Lagrangian statistics of the turbulent flow for each simulation, the trajectories of 1.2×10^5 fluid points, released at $t=5$, are tracked in time within the three-dimensional computational domain surrounding the solid particles. The instantaneous Lagrangian velocity of the fluid point, required to integrate its trajectory, is computed using the fourth-order three-dimensional Hermite interpolation (Ferrante 2004) from the fluid velocity at the eight Eulerian grid nodes surrounding the fluid point.

It is important to note that resolving the flow around the moving particles using the IB method is computationally efficient as compared to other methods. The simulations, performed on 128 cores of IBM Blue-GeneL, of the single-phase flow and the particle-laden flow (with 6400 particles each represented by 198 Lagrangian points, for a total of 1.3 million Lagrangian points; 1.2×10^5 fluid points to compute the Lagrangian statistics) required 6 and 12 clock hours, respectively, to advance the solution in time for 10 240 time steps.

3.3. *Turbulence modification by particles*

In the following subsection we provide an overview of the effects of the particles on the temporal decay of TKE. In § 3.3.2, we describe in detail the physical mechanisms by which the different particles modify the dissipation rate, $\varepsilon(t)$, and the two-way coupling rate of change of TKE, $\Psi_p(t)$, and, in turn, affect the rate of decay of TKE. The effects of the particles on the frequency spectrum of TKE are discussed in § 3.3.4.

B	C	D	E	F	G	H
1.2	7.9	16.3	22.7	26.3	14.6	8.6

TABLE 4. Percentage reduction of TKE relative to case A at $t = 8$.

3.3.1. *Turbulence kinetic energy*

Figure 9 shows the temporal development of the TKE normalized by its initial value, $E(t)/E_0$, for the nine cases (A to H) studied. It is seen that the particles in all cases B to H increase the decay rate of TKE with respect to that of single-phase flow (case A) for $1.2 \leqslant t \leqslant 3$. However, as a particle is released in the flow, its surface displaces and deforms the surrounding fluid, thus resulting in a slight increase in TKE, relative to case A, as shown in figure 9 for case F with the largest mass fraction, $\phi_m = 1$, during $1 \leqslant t \leqslant 1.2$. At later times, $t > 3$, the TKE of cases B to H stays smaller than that of case A. The decay rate of TKE increases monotonically by increasing the particle volume fraction from zero to 0.1 (cases A–D) or decreasing the particle diameter (cases H, G and D). Increasing the particle-to-fluid density ratio from 2.56 to 10 (cases D–F), all three cases increase the decay rate of TKE, but there is no clear monotonicity. The decay rate of TKE is increased by increasing the mass fraction from 0 to 1 (cases A–F). At $t = 8$, the TKE is 16 % smaller in case D, 13 % in case E, and 26 % in case F with respect to that in case A. Table 4 shows the percentage reduction of TKE relative to case A.

It should be noted that the diameter of the particles is one order of magnitude larger than η, $16 \leqslant d/\eta \leqslant 35$, and their response time is two orders of magnitude larger than τ_k, $38 \leqslant \tau_p/\tau_k \leqslant 178$ (at time $t = 1$). The decay of TKE is due to the combined effects of viscous dissipation and two-way coupling:

$$\frac{\mathrm{d}E(t)}{\mathrm{d}t} = -\varepsilon(t) + \Psi_p(t), \tag{3.3}$$

where $\varepsilon(t)$ is the viscous dissipation rate of TKE (figures 10 and 11 to be discussed below):

$$\varepsilon(t) = 2\nu \left\langle s_{ij} s_{ij} \right\rangle, \tag{3.4}$$

with $s_{ij} = (\partial_j u_i + \partial_i u_j)/2$, the strain-rate tensor. Note that $\Psi_p(t)$ is the two-way coupling rate of change of TKE due to the forces exerted by the particle surface on its surrounding fluid (figure 12)

$$\Psi_p(t) = \left\langle u_i f_i \right\rangle, \tag{3.5}$$

where $\langle \ldots \rangle$ denotes ensemble averaging throughout the computational domain outside the immersed boundaries of the solid particles. Note that $\Psi_p(t)$ can act as a source or sink of TKE as was shown by Ferrante & Elghobashi (2003), whereas $\varepsilon(t)$, by definition, is always a sink of TKE.

It should also be noted that since the prescribed density ratio $\rho_p/\rho_f = 2.56$, 5.0 and 10, i.e. $\leqslant 10$, all forces acting on the particle become important, in contrast to the case of large density ratio ($\sim 10^3$) for which the drag force predominates. Furthermore, for finite-size particles with diameter larger than the Kolmogorov length scale, η, all forces become important, and thus the particle response time is not the only parameter that determines the particle motion and the two-way coupling effects through the Stokes number, τ_p/τ_k, as is the case for particles with diameter smaller than η. Our DNS results of cases E and G show that particles with nearly the same inertia ($\tau_p/\tau_k \simeq 74$)

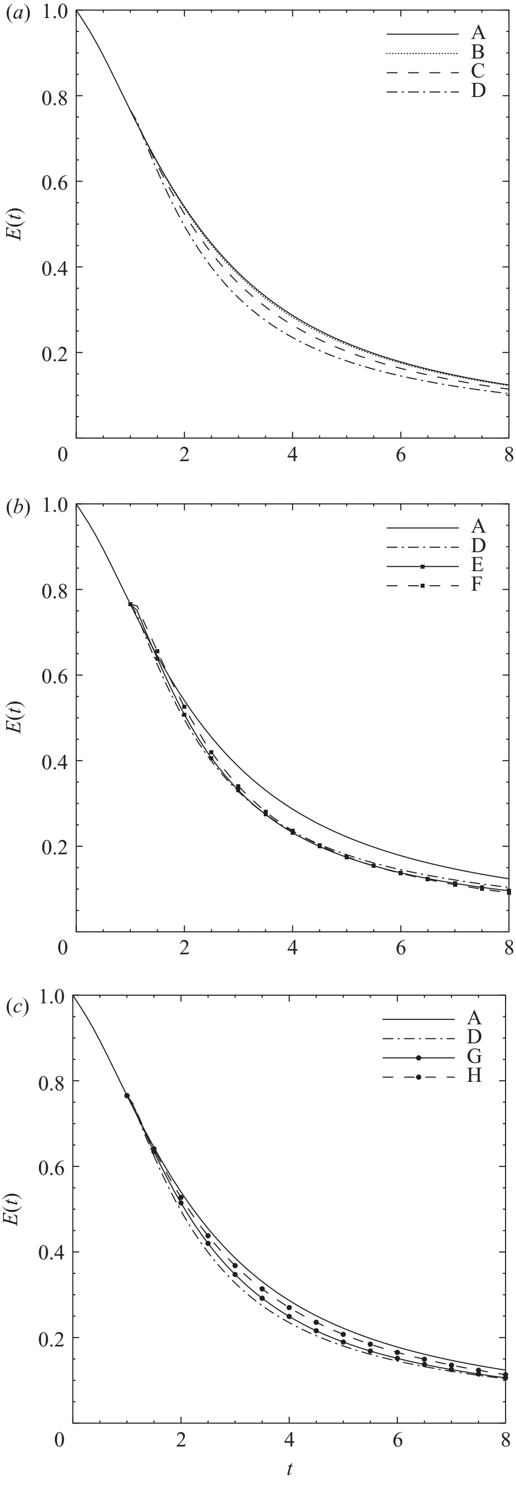

FIGURE 9. Temporal development of the turbulence kinetic energy normalized by its initial value.

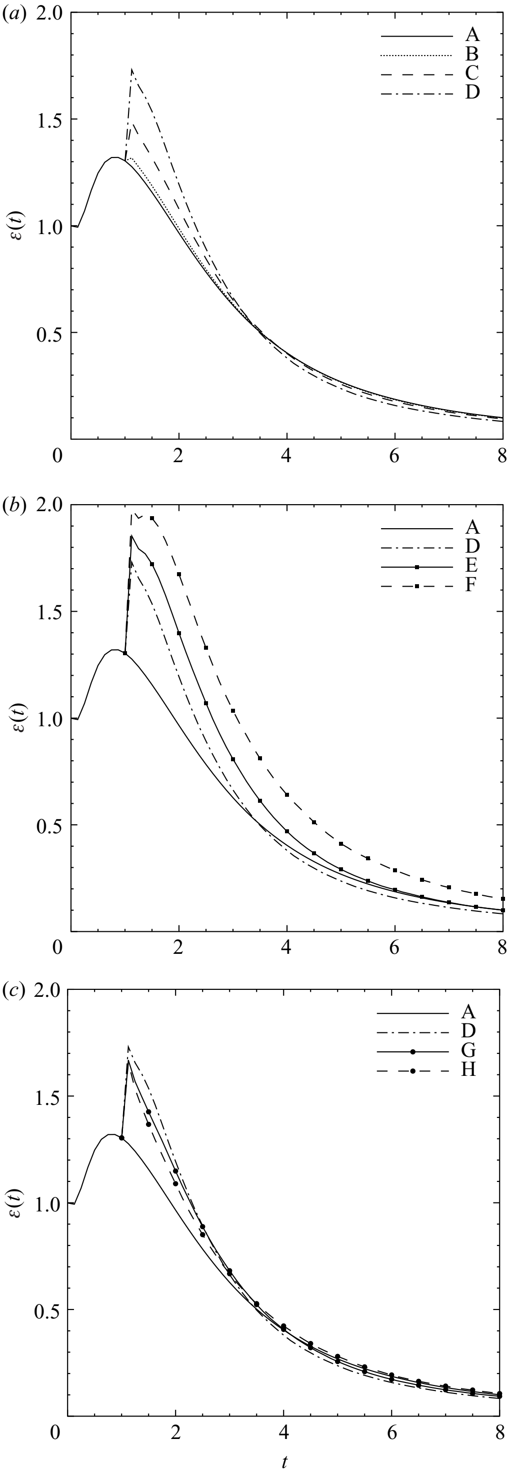

FIGURE 10. Temporal development of the viscous dissipation rate of turbulence kinetic energy normalized by its initial value.

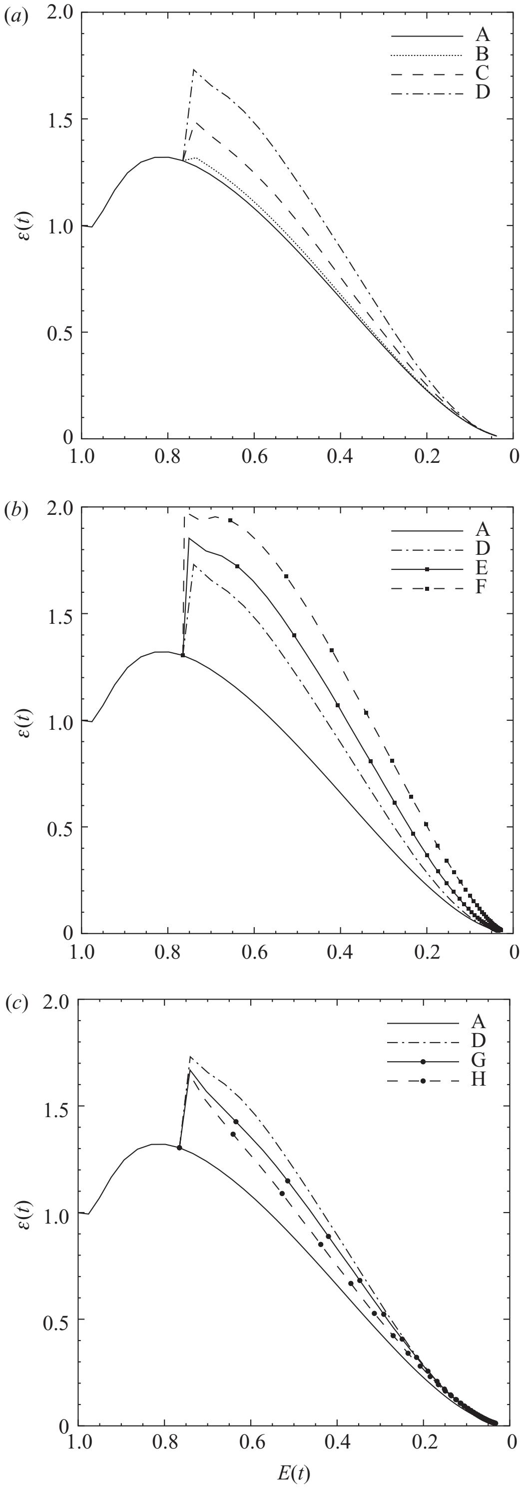

FIGURE 11. Viscous dissipation rate of turbulence kinetic energy normalized by its initial value versus turbulence kinetic energy.

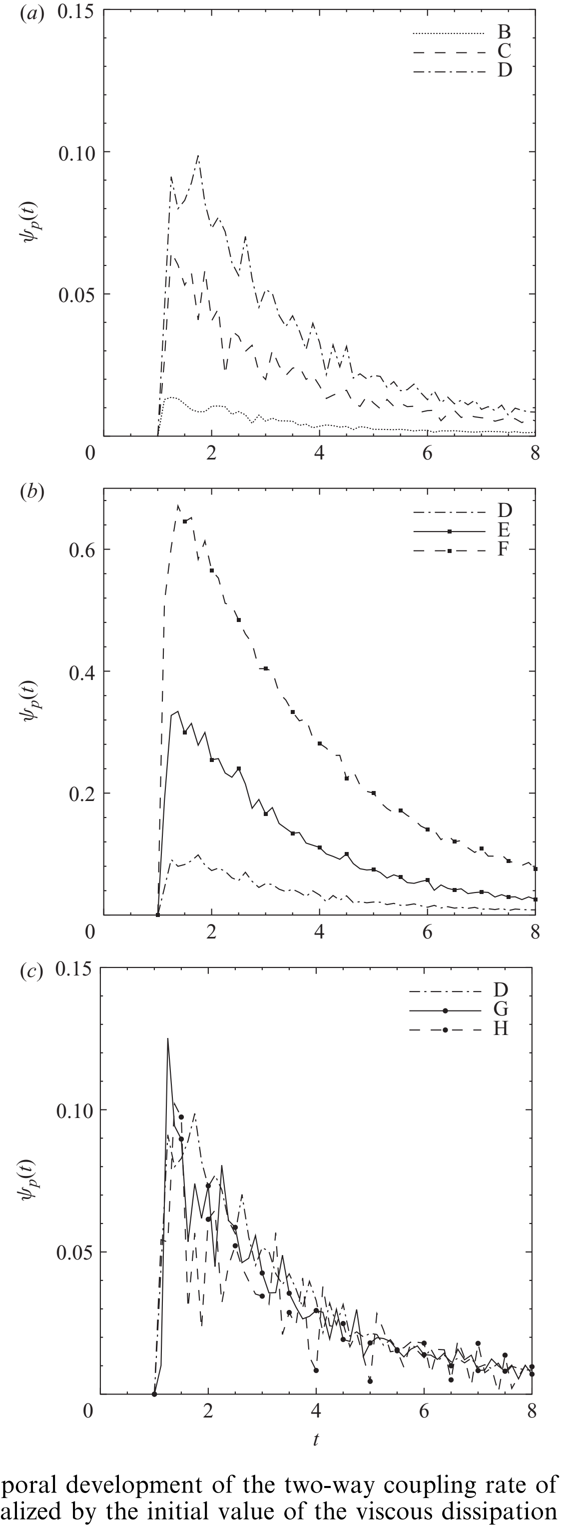

FIGURE 12. Temporal development of the two-way coupling rate of change of TKE normalized by the initial value of the viscous dissipation rate.

and same volume fraction ($\phi_v = 0.1$), but different diameters and densities (or mass fraction), have different effects on $E(t)$, $\varepsilon(t)$ and $\Psi_p(t)$ as shown in figure 13. The reason is provided in the next subsection.

3.3.2. *Dissipation rate of TKE and two-way coupling rate of change of TKE*

Figure 10 shows the temporal development of the dissipation rate of TKE, $\varepsilon(t)$. In all particle-laden cases, $\varepsilon(t)$ immediately peaks higher than that of case A when particles are introduced into the flow ($t = 1$). For example, in case F, $\varepsilon(t)$ increases by about 56 % above case A at $t = 1$. This augmentation of $\varepsilon(t)$ increases with mass fraction from case B to case F. Increasing particle diameter while keeping the same volume and mass fraction (cases D, G and H) reduces the peak of $\varepsilon(t)$ at $t = 1$ and maintains the differences between these three cases at early times after injection ($1 < t < 3$), but reverses that trend at later times ($t > 3$). In all particle-laden cases, except in case F for $t \leqslant 20$, there is a crossover in their $\varepsilon(t)$ with that of case A. The time of the crossover increases with increasing the mass fraction (figure 10). The crossover in the $\varepsilon(t)$ is due to the decay of TKE (figure 9). In all particle-laden cases, $\varepsilon(t)$ is larger than that of single-phase flow (case A) for any value of TKE as shown in figure 11. It is seen that $\varepsilon(E)$ increases with volume fraction (cases A–D), particle-to-fluid density ratio (cases A, D, E and F) or mass fraction (cases A–F), and for decreasing diameter (cases H, G and D; figure 11).

The two-way coupling rate of change of TKE, $\Psi_p(t)$, is zero for single-phase flow ($f_i = 0 \rightarrow \Psi_p(t) = 0$), and positive in particle-laden cases (figure 12), i.e. $\Psi_p(t)$ acts as a source of TKE. The maximum value of $\Psi_p(t)$ occurs at the time of particle release in the flow followed by a decay in time as turbulence decays. Note that $\Psi_p(t)$ increases with volume fraction, and particle-to-fluid density ratio (or mass fraction), and its value is about 10 %, 25 % and 50 % of $\varepsilon(t)$ in cases D, E and F (figure 14), respectively. Varying the particle diameter for a fixed volume fraction and mass fraction does not change $\Psi_p(t)$ significantly (cases D, G and H in figure 12). However, the ratio $\Psi_p(t)/\varepsilon(t)$ decreases slightly with increasing the particle diameter (cases D, G and H) as shown in figure 14. The amplitude of the wiggles of $\Psi_p(t)$ is larger in case H because of the effects of the repulsive force (2.22), large particle inertia and smaller number of particles. As two particles approach each other, a repulsive force, $\boldsymbol{F}_R^{(m)}$, is imposed on them to avoid overlapping. The resulting acceleration produces a force, f_i, on the surrounding fluid. In case H, this force is large due to the large particle inertia, $\tau_p/\tau_k = 178$, which in turn produces a large $\Psi_p(t)$. The oscillations in $\Psi_p(t)$ are caused by ensemble averaging over a smaller number of particles ($Np = 640$) due to a larger particle diameter for a fixed volume fraction. In the next two subsections, an explanation is provided of how finite-size particles increase the dissipation rate and generate a positive two-way coupling rate of change of TKE.

Dissipation rate of TKE

The presence of solid particles in the turbulent flow introduces, through the no-slip condition at the particle surface (Lagrangian points), a local force, f_i, on the fluid surrounding the particle. This force increases the velocity gradients, $\partial_j u_i$, close to the particle surface, thus increasing the local strain rate, s_{ij}. Figures 15–17 show the mean square strain rate, $\overline{s_{ij}s_{ij}}$, as a function of the distance, r, from the surface of the closest particle, for the region in front and back (wake) of the particle in the sets of cases BCD, DEF and DGH, respectively, at $t = 2$. The overline '$\overline{\cdots}$' denotes instantaneous ensemble average over a subset of Eulerian grid points. The subset depends on the position of the Eulerian grid point and its closest particle velocity.

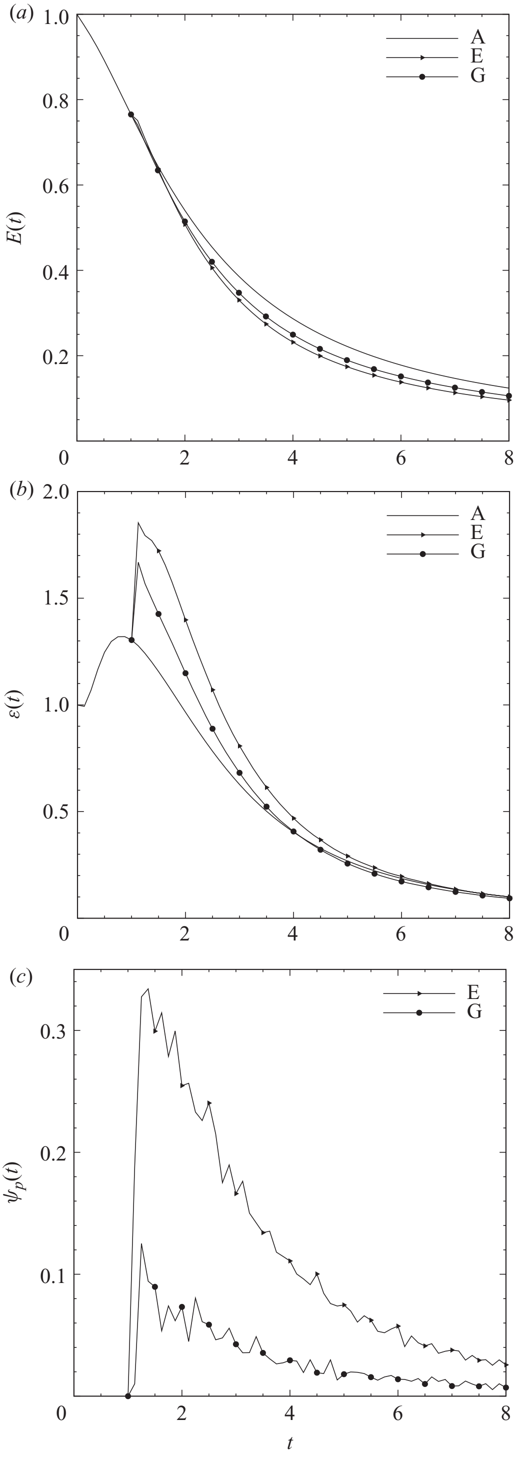

FIGURE 13. Temporal development of TKE, $E(t)$, dissipation rate of TKE, $\varepsilon(t)$, and two-way coupling rate of change of TKE, $\Psi_p(t)$, normalized by their initial values in cases A, E and G.

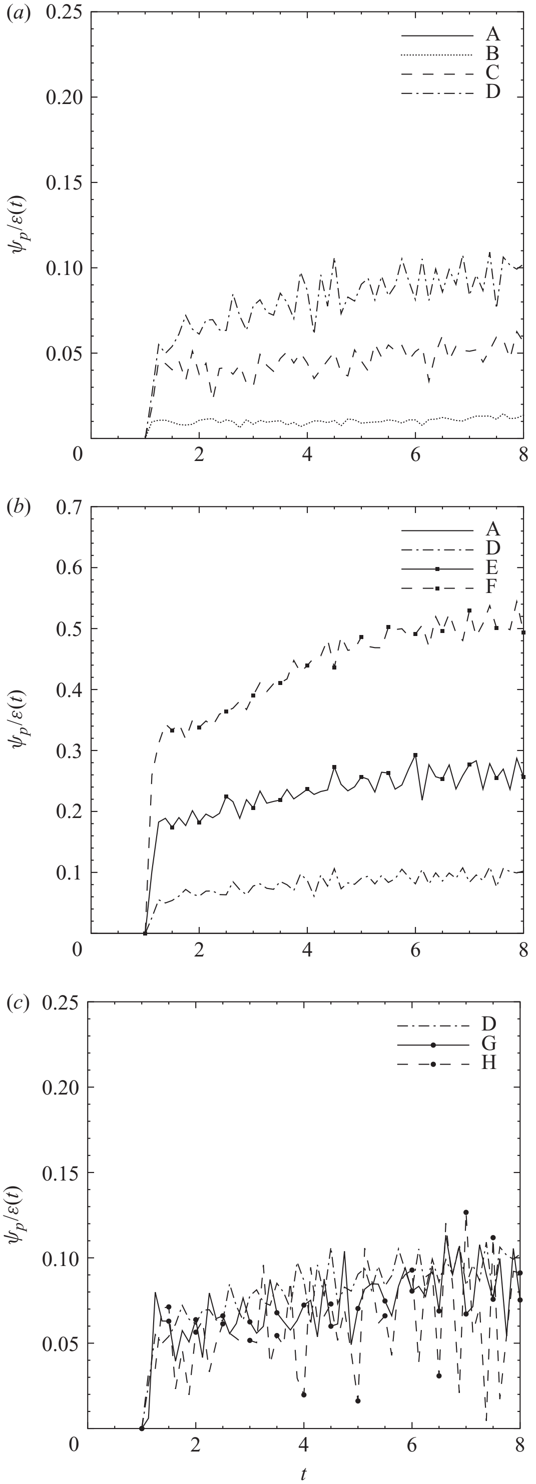

FIGURE 14. Two-way coupling rate of change of TKE and viscous dissipation ratio versus time.

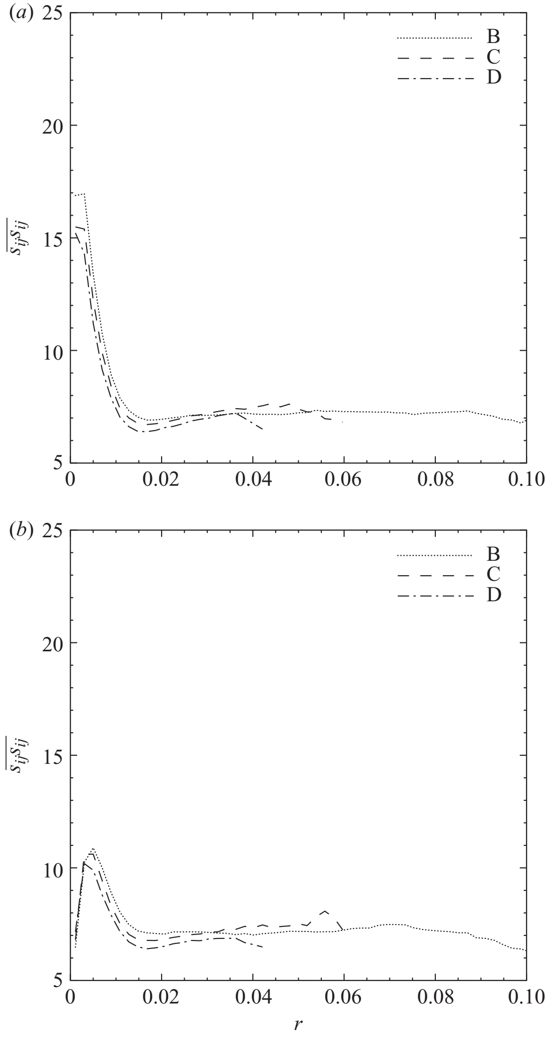

FIGURE 15. Mean square strain rate, $\overline{s_{ij}s_{ij}}$, versus distance from the closest particle, r, region in the front of the particle (a) and region in the back of the particle (b) in cases B–D.

The front (or back) of the particle is defined as the sub-domain where $(\boldsymbol{x} - \boldsymbol{x}_p) \cdot \boldsymbol{v} > 0$ (or < 0). In the front of the particle, $\overline{s_{ij}s_{ij}}$ at the closest Eulerian points to the particle surface is few times higher than farther away ($r \geqslant d$).

Figure 15 shows that $\overline{s_{ij}s_{ij}}$ does not change significantly with varying the volume fraction but fixed particle diameter and density ratio in cases B–D. In contrast, $\overline{s_{ij}s_{ij}}$ increases with the particle-to-fluid density ratio for a fixed particle diameter and volume fraction (cases D–F) as shown in figure 16. For example, consider the closest point to the particle surface in case F. Compared to $\overline{s_{ij}s_{ij}}$ at a distance of one particle diameter ($r = d = 0.03$), $\overline{s_{ij}s_{ij}}$ is about 4.3 times larger in the front of the particles and 2 times larger in the back of the particles. Particles with largest diameter (case H) have higher inertia than smaller particles (case D), $\tau_{p,H} \simeq 4.7\tau_{p,D}$ and thus they induce larger local shear in the fluid surrounding the particle. Thus, increasing the

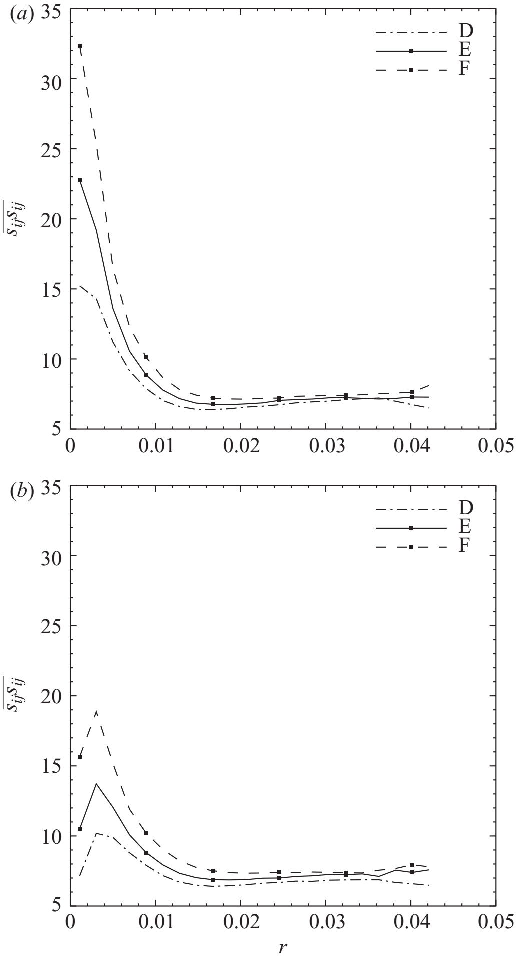

FIGURE 16. Mean square strain rate, $\overline{s_{ij}s_{ij}}$, versus distance from the closest particle, r, region in the front of the particle (a) and region in the back of the particle (b) in cases D–F.

particle diameter (cases D, G and H) increases $\overline{s_{ij}s_{ij}}$ at the nearest point to the front particle surface (figure 17).

The larger increase of the strain rate in the front rather than in the back of the particles is due to the fact that, while freely moving, each particle pushes the fluid forward, whereas in the back of the particle, the fluid is attracted towards the wake of the particle by the induced pressure gradient. The augmentation of $\overline{s_{ij}s_{ij}}$ increases the magnitudes of the extensional (α) and compressive (γ) eigenvalues of the velocity gradient tensor in the flow surrounding the particles relative to single-phase flow. Figures 18–20 show the eigenvalues $\overline{\alpha}$, $\overline{\beta}$ and $\overline{\gamma}$, respectively, as function of the distance, r, from the particle surface. The extensional and compressive eigenvalues, $\overline{\alpha}$ and $\overline{\gamma}$, are larger near the particle surface than farther away. This effect is more pronounced in the front of the particle than in the back. Note that $\overline{\beta}$ has smaller magnitude than $\overline{\alpha}$ and $\overline{\gamma}$, thus its contribution to $\overline{s_{ij}s_{ij}} = \overline{\alpha^2 + \beta^2 + \gamma^2}$ is less important than that of $\overline{\alpha}$ and $\overline{\gamma}$. Table 5 shows that in case F the mean magnitudes of α and γ are 17 % and 14 % higher than those of case A at $t = 2$. Figures 21–23 show that the probability density functions (p.d.f.s) of α, β and γ exhibit extended tails with

	A	B	C	D	E	F	G	H
ω_{rms}	4.28	4.29	4.34	4.31	4.6	4.97	4.36	4.35
$\langle \omega^2 \rangle$	18.29	18.37	18.82	18.55	21.2	24.66	19.02	18.91
$\langle S_{ij}S_{ij} \rangle$	7.12	7.18	7.46	7.5	8.6	10.08	7.58	7.45
$\langle \alpha^2+\beta^2+\gamma^2 \rangle$	7.12	7.18	7.46	7.5	8.6	10.08	7.58	7.45
$\langle \alpha \rangle$	1.55	1.55	1.58	1.58	1.69	1.81	1.59	1.58
$\langle \beta \rangle$	0.17	0.16	0.15	0.13	0.14	0.14	0.14	0.15
$\langle \gamma \rangle$	−1.71	−1.71	−1.73	−1.71	−1.82	−1.95	−1.73	−1.73

TABLE 5. Averaged statistics over the Eulerian grid points of the flow outside the particles at time $t=2$ of vorticity, ω, strain rate, s_{ij}, and eigenvalues of the velocity gradient tensor, α, β and γ.

significant magnitudes for all the particle-laden cases than in case A. These p.d.f.s indicate that the intermittent large magnitude strain rates correspond to the sheared flow surrounding the moving particles. The fluid elements in front of the freely moving spherical particles are stretched in the direction tangential to the particle surface and compressed in the direction normal to the particle surface by the induced velocity field surrounding the particle surface. Figure 24 shows the increased (red colour) extensional and compressive eigenvalues, α and γ, to be more pronounced in the front side of the spheres than in the back. It should be noted that the spherical particles in figure 24 appear to be of different sizes. This is only because the plane intersects with the uniform size particles while they are moving in the third direction (perpendicular to the plane). Figure 25 and the animation (supplementary movie 1 available at journals.cambridge.org/flm) show the instantaneous two-dimensional contours of $s_{ij}s_{ij}$ in a sub-region of the computational domain. The TKE dissipation rate, $\varepsilon(t)$, is proportional to $\langle s_{ij}s_{ij}\rangle$ via (3.4). Thus, $\varepsilon(t)$ increases in the particle-laden cases relative to that in case A as discussed above with a bias in the downstream direction to their motion (front of the particle). The increase of $s_{ij}s_{ij}$ in the zone surrounding the particle reduces the instantaneous TKE relative to that of single-phase flow (figure 25 and Movie 2). In all cases studied, the particles do not generate turbulent wakes since the particle Reynolds number is less than 90 in cases B to G, and smaller than 170 in case H. Thus, particles increase the local shear, close to their surface in the direction of their motion, and increase the vorticity also in the back region of the particle but not as intensely as in the front region, as shown by the two-dimensional (x–z plane) instantaneous contours of ω_y vorticity component (figure 25 and Movie 3).

The effects of particles on TKE, ε and Ψ_p are more pronounced for larger mass fraction, ϕ_m, of the particles (cases D–F in figures 9, 10 and 12). Figure 26 shows, for cases D–F, the profiles of the magnitude of the difference between the fluid and the particle velocity vectors, $|\overline{\boldsymbol{u}-\boldsymbol{v}}|$, ensemble averaged for the Eulerian points in front of the particle, as a function of the distance, r, from the closest particle surface. For heavier particles (case F, $\rho_p/\rho_f=10$), the average velocity difference is larger than that for lighter particles (case D, $\rho_p/\rho_f=0.256$). Also, figure 27 shows the average scalar product of the fluid and the particle velocity vectors, $\overline{\boldsymbol{u}\cdot\boldsymbol{v}}/|\boldsymbol{u}||\boldsymbol{v}|=\cos(\theta)$, where θ is the average angle formed between the two velocity vectors. The angle θ measures the alignment between the particle velocity and the average velocity of its surrounding fluid. For example, if $\theta=0°$, the particle follows the surrounding fluid averaged

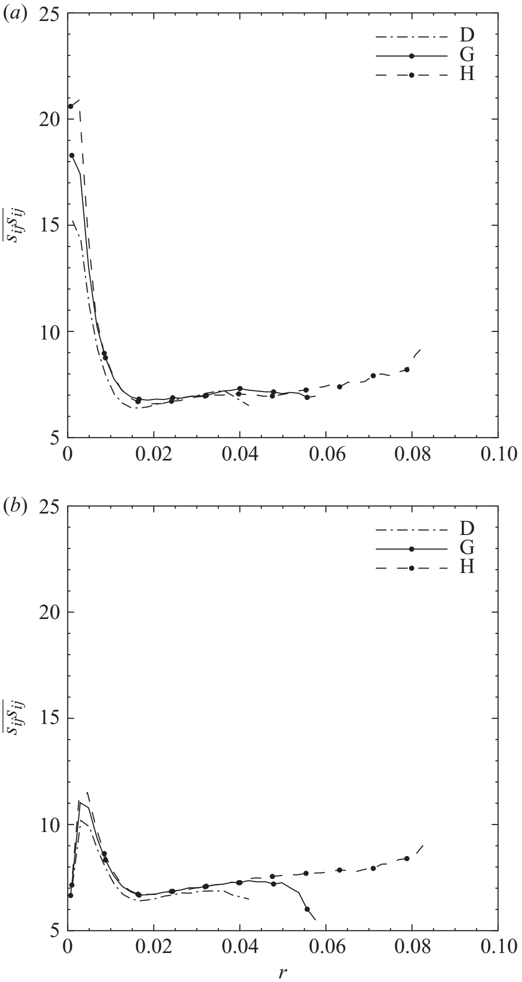

FIGURE 17. Mean square strain rate, $\overline{s_{ij}s_{ij}}$, versus distance from the closest particle, r, region in the front of the particle (a) and region in the back of the particle (b) in cases D, G and H.

motion, and if $\theta = 90°$ the particle crosses perpendicularly the surrounding averaged fluid velocity. Close to the particle surface, $\overline{\boldsymbol{u} \cdot \boldsymbol{v}/|\boldsymbol{u}||\boldsymbol{v}|} \simeq 1$ (i.e. $\theta = 0°$) due to the no-slip condition at the boundary (figure 27). Particles with larger inertia (τ_p), cases F and H, have smaller $\overline{\boldsymbol{u} \cdot \boldsymbol{v}}$, i.e. larger deviation angle θ. Figures 26 and 27 show that particle trajectories in cases F and H deviate more from the motion of the surrounding fluid as compared with lighter particles. The schematic in figure 28 shows the effect of particle inertia on the particle and fluid velocity vectors. Particles with higher inertia (τ_p), case F, are less dependent on the surrounding fluid motion, thus deviating more from the surrounding fluid trajectories (figure 26). This larger velocity difference between the particle and the surrounding fluid induces larger forcing on the surrounding fluid and increases the local shear rate and dissipation rate of TKE around particles than particles with smaller τ_p (case D). In summary, particles in case F induce larger effects on TKE (ε and Ψ_p) than particles in case D (figures 9, 10 and 12).

The larger shear and dissipation rates in the front of the particles than those in the back are manifested in figure 27, which shows that $\overline{\boldsymbol{u} \cdot \boldsymbol{v}}$ is larger in the back than in

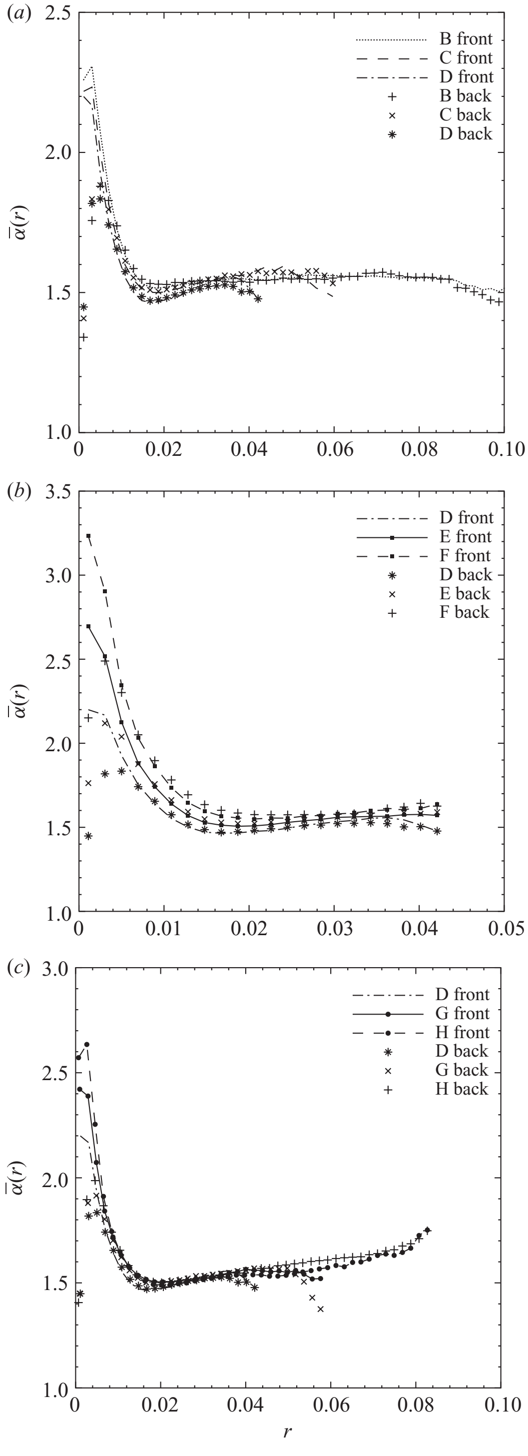

FIGURE 18. Local stretching eigenvalue of the strain rate tensor, α, versus distance from the closest particle, region in front of the particle (front) and region in the front of the particle (*a*), and region in the back of the particle (*b*).

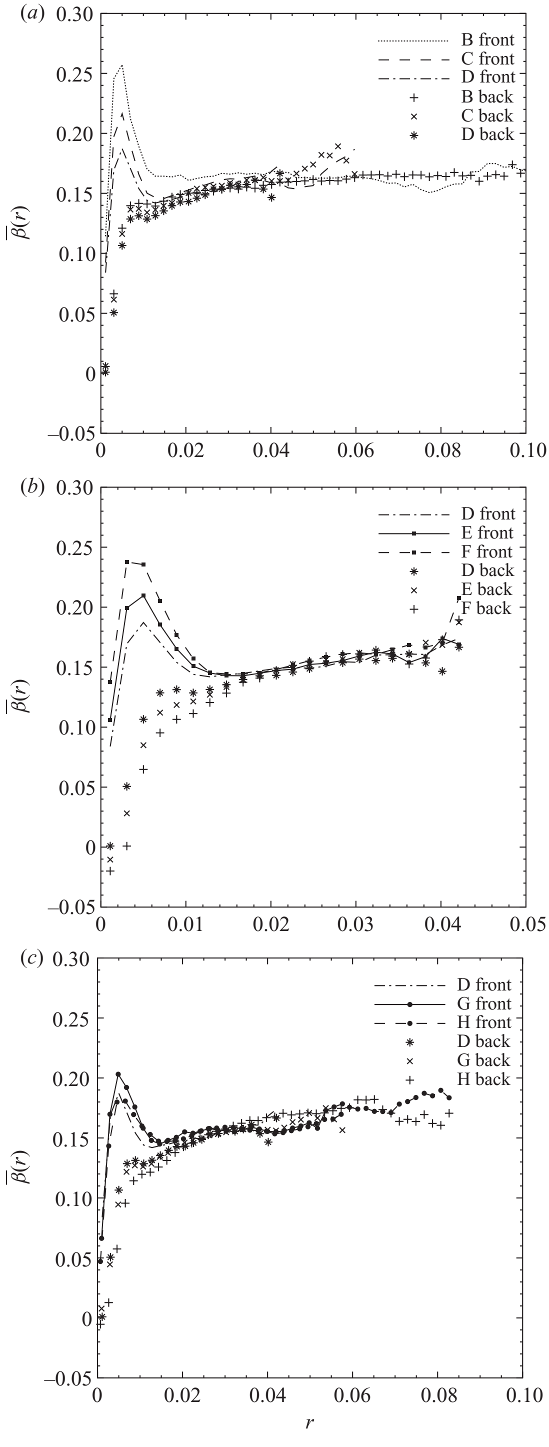

FIGURE 19. Local intermediate eigenvalue of the strain rate tensor, β, versus distance from the closest particle, region in front of the particle (front) and region in the back of the particle (back).

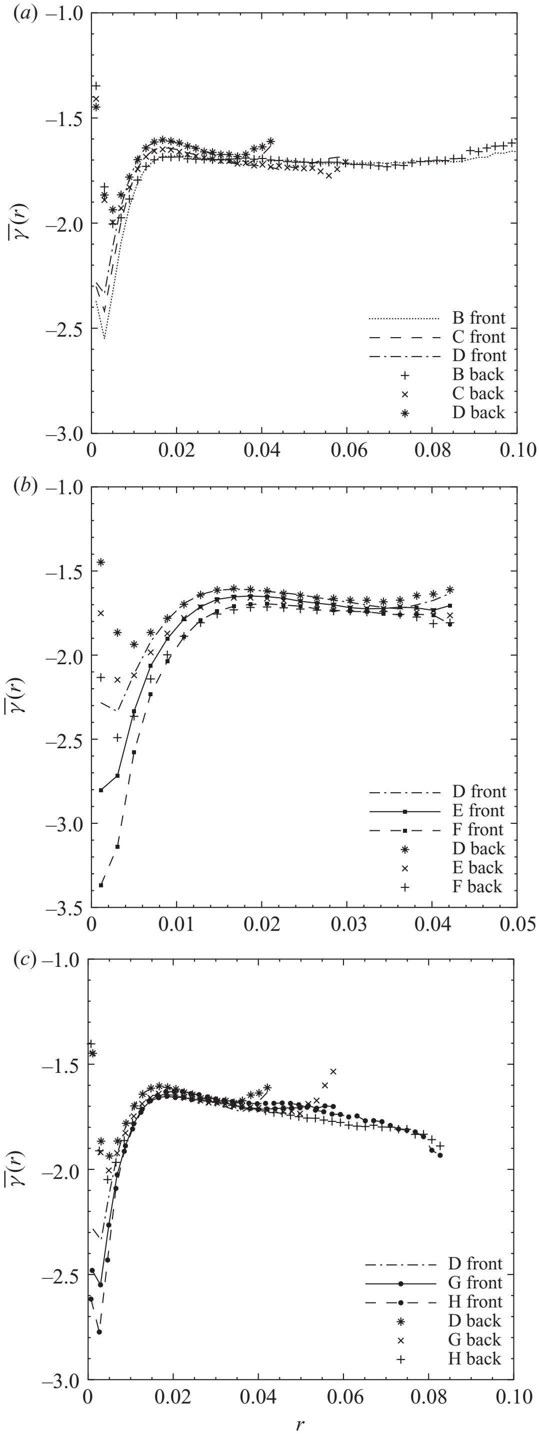

FIGURE 20. Local compressive eigenvalue of the strain rate tensor, γ, versus distance from the closest particle, region in front of the particle (front) and region in the back of the particle (back).

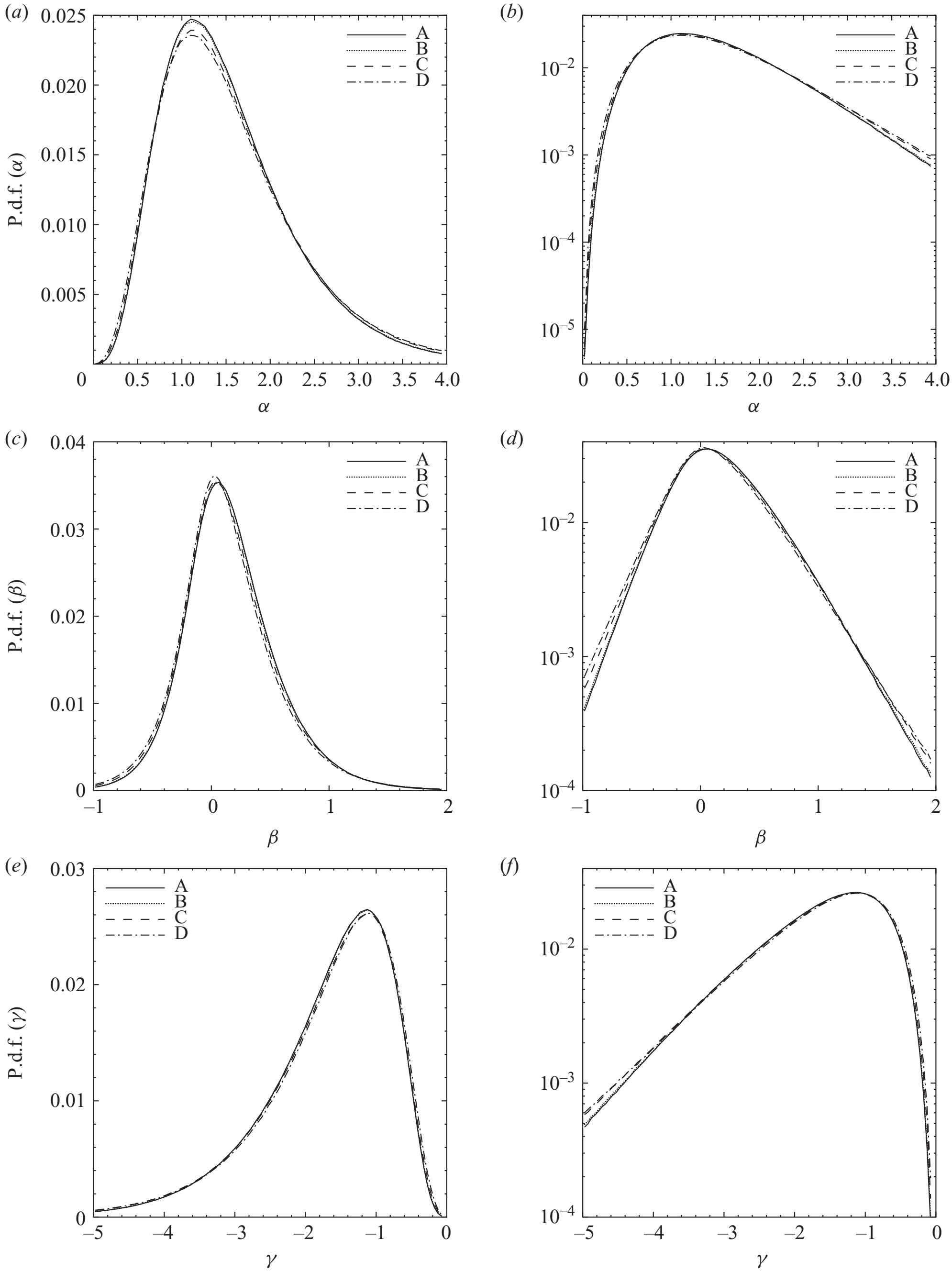

FIGURE 21. P.d.f. of α, β and γ, with linear (*a,c,e*) and log-normal (*b,d,f*) scales at $t = 2.0$ in cases A–D.

the front of the particle. The velocity of the particle and surrounding fluid are more aligned in the back than in the front of the particle.

Figure 13 shows that particles with nearly the same inertia ($\tau_p \simeq 11$ in cases E and G) and the same volume fraction ($\phi_v = 0.1$), but different diameters and densities (or mass fraction), have different effects on $E(t)$, $\varepsilon(t)$ and $\Psi_p(t)$. Smaller and heavier

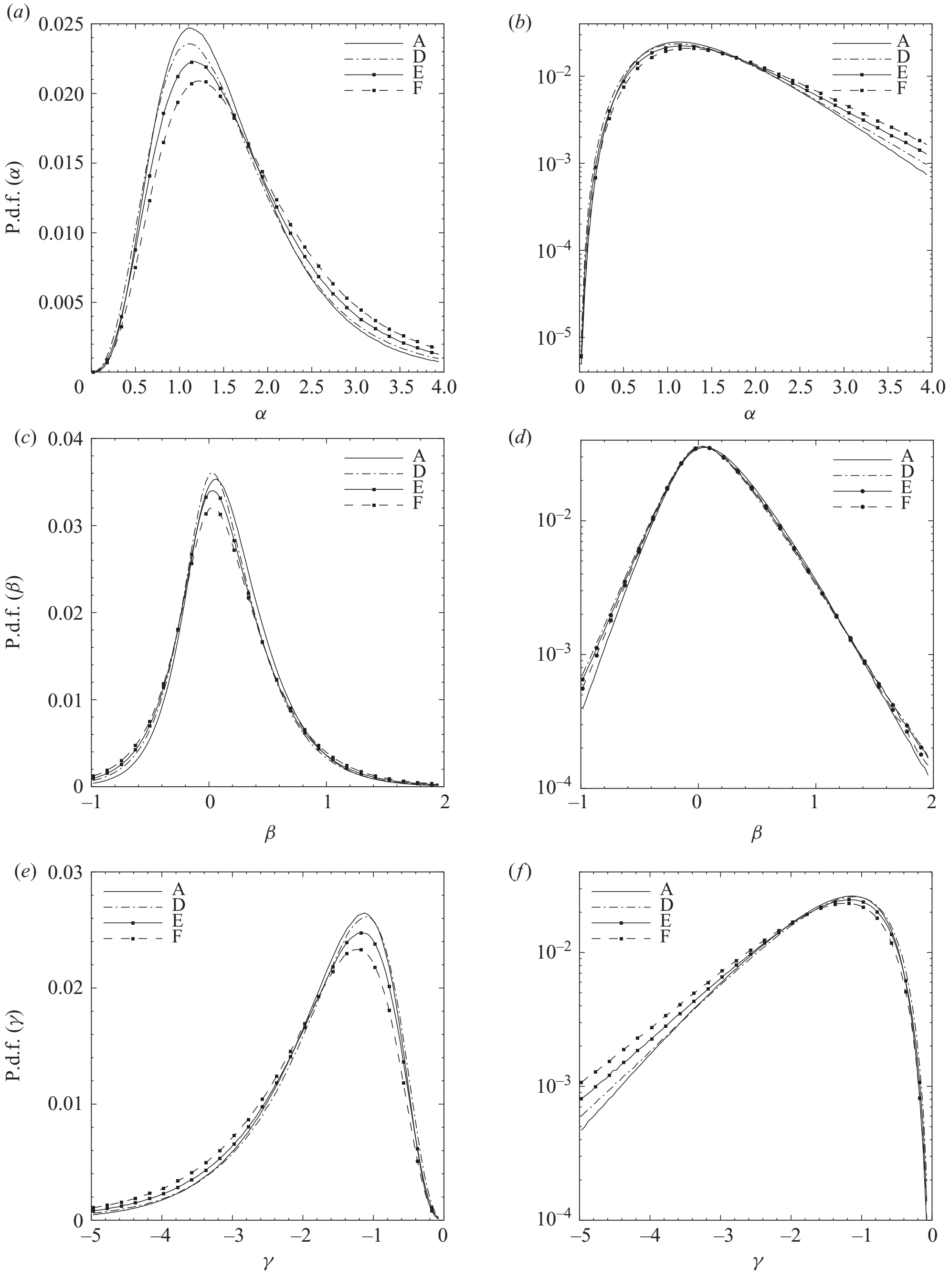

FIGURE 22. P.d.f. of α, β and γ, with linear (*a,c,e*) and log-normal (*b,d,f*) scales at $t = 2.0$ in cases A and D–F.

particles (case E) reduce TKE and increase $\varepsilon(t)$ and $\Psi_p(t)$ more than larger and lighter particles (case G). The larger reduction of TKE is due to the increase in $\varepsilon(t)$, which overcomes the increase of $\Psi_p(t)$. The increased enhancement of $\varepsilon(t)$ is due to the increase (44 %) of total particle surface immersed in the flow field from case G to case E.

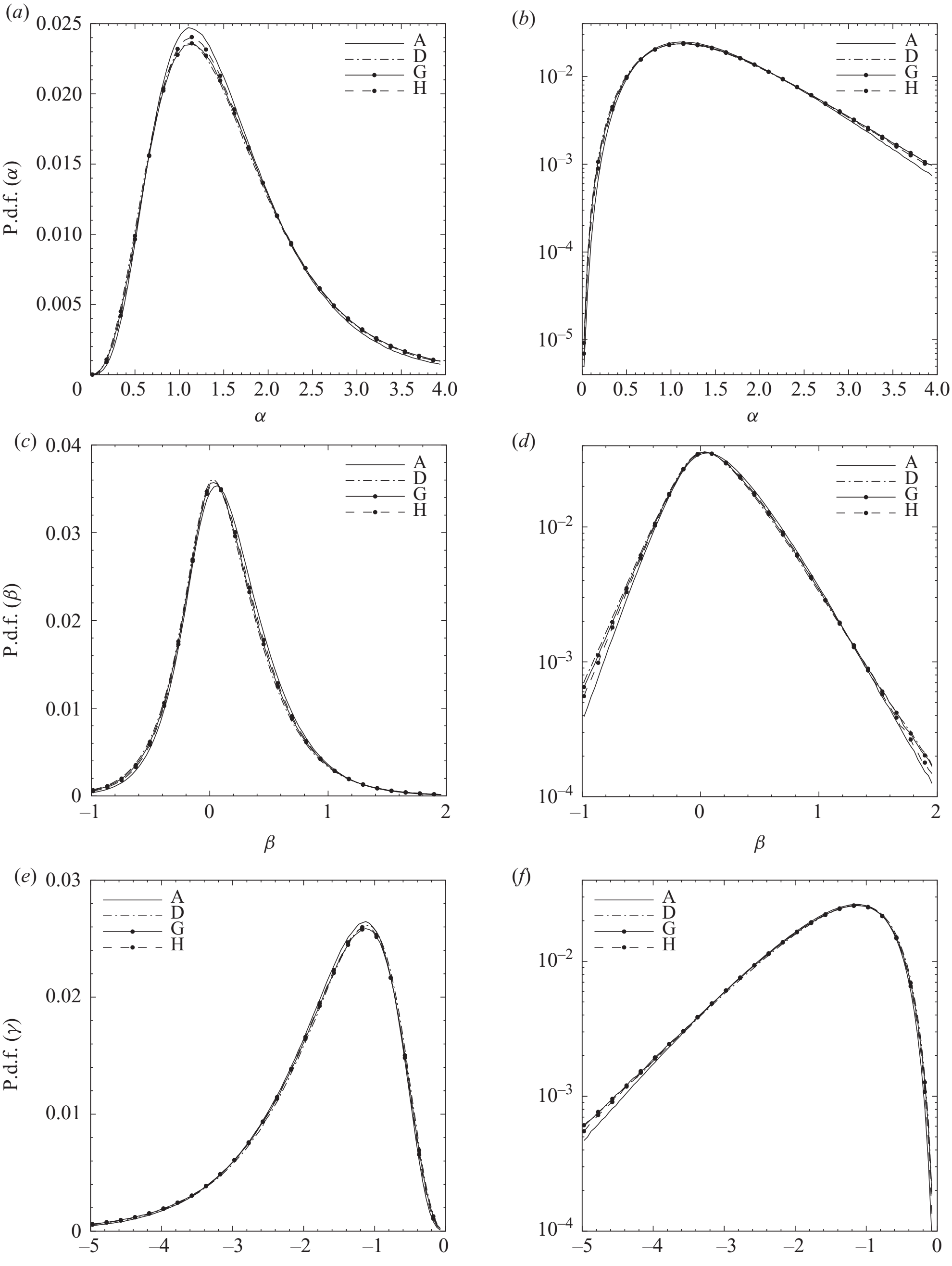

FIGURE 23. P.d.f. of α, β and γ, with linear (*a,c,e*) and log-normal (*b,d,f*) scales at $t = 2.0$ in cases A, D, G and H.

Two-way coupling effects on TKE

The question of how finite-size particles induce a positive $\Psi_p(t)$ is now addressed. The particles are immersed in an isotropic turbulent flow which exerts surface forces on the particles. The particles, in turn, impart a reaction surface force, f_i, on the

	B	C	D	E	F	G	H
$\theta_{uf} < 90^\circ$ (%)	42.6	43.1	43.4	44.5	46.2	43.7	44.6
$\overline{\lvert \boldsymbol{f} \rvert}(\theta_{uf} < 90^\circ)$	0.0768	0.0858	0.0989	0.1220	0.1583	0.0947	0.0910
$\overline{\lvert \boldsymbol{f} \rvert}(\theta_{uf} > 90^\circ)$	0.0548	0.0631	0.0756	0.0868	0.1079	0.0707	0.0691
$\overline{\lvert \boldsymbol{u} \rvert}(\theta_{uf} < 90^\circ)$	0.0536	0.0520	0.0511	0.0525	0.0547	0.0502	0.0498
$\overline{\lvert \boldsymbol{u} \rvert}(\theta_{uf} > 90^\circ)$	0.0547	0.0538	0.0528	0.0539	0.0553	0.0519	0.0507

TABLE 6. Percentage of Eulerian grid points of the flow outside the particles where $\theta_{uf} < 90^\circ$, and $\overline{|\boldsymbol{f}|}$ and $\overline{|\boldsymbol{u}|}$ for θ_{uf} larger or smaller than 90°.

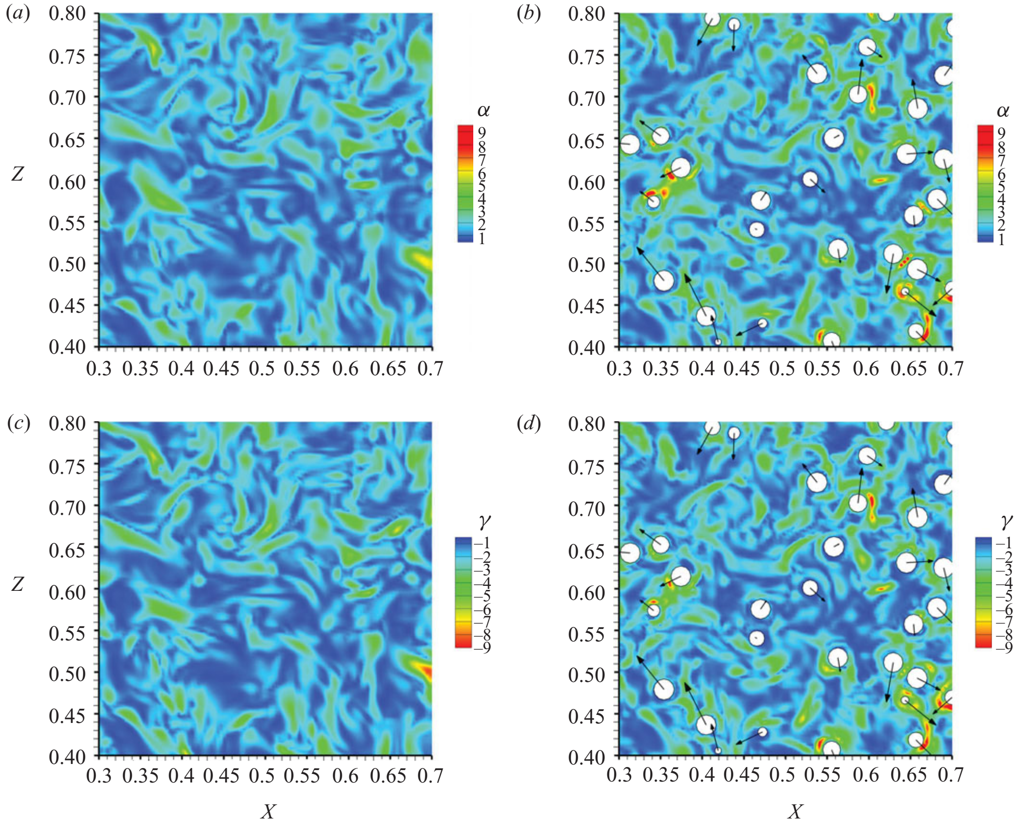

FIGURE 24. Instantaneous contours in x–z plane of α and γ for cases A (a,c) and F (b,d) at $t = 2.0$.

surrounding fluid. Each moving particle drags the surrounding fluid via the local force f_i. Figure 29 shows that the fluid surrounding the particle is subjected to a local force f_i (white arrows). Table 6 shows that in $\sim 45\,\%$ of the points where $\boldsymbol{f}$ is not zero, the angle θ_{uf}, between the fluid velocity, $\boldsymbol{u}$, and forcing vectors, $\boldsymbol{f}$, is, on the average, smaller than 90°. Figure 30 shows that the magnitude of the two-way coupling force, $\overline{|\boldsymbol{f}|}$, ensemble averaged over the Eulerian points where it is finite, decreases with θ_{uf} ($0^\circ \leqslant \theta_{uf} \leqslant 180^\circ$). Accordingly, table 6 shows that the magnitude of $\boldsymbol{f}$ ensemble averaged for the points where $\theta_{uf} < 90^\circ$ is larger than its value if averaged where

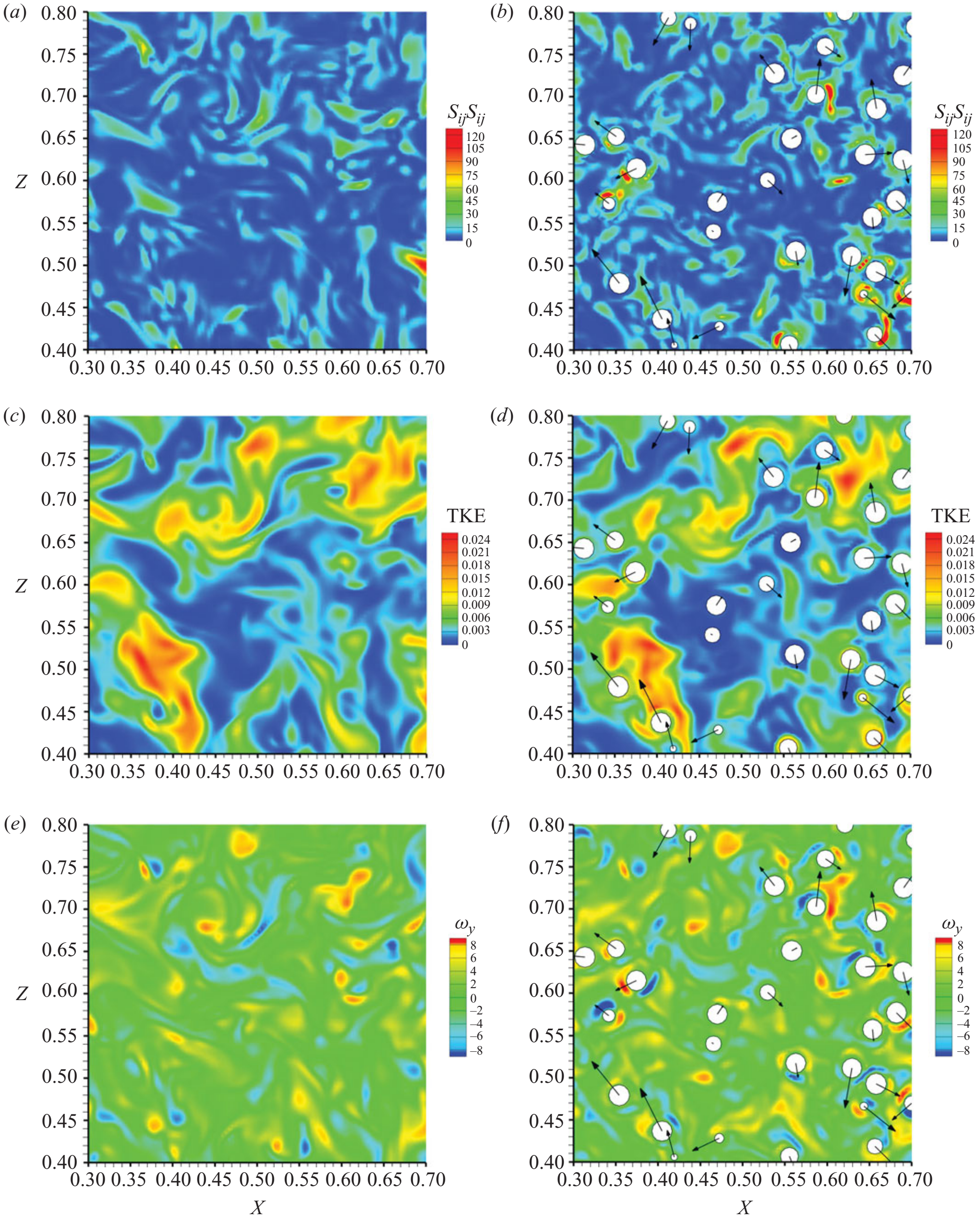

FIGURE 25. Instantaneous contours in x–z plane of $s_{ij}s_{ij}$, TKE and ω_y for cases A (*a*,*c*,*e*) and F (*b*,*d*,*f*) at $t = 2.0$.

$\theta_{uf} > 90°$, and the magnitude of $\boldsymbol{u}$ does not change much for θ_{uf} larger or smaller than 90°.

The net result of these two opposing effects is that $\boldsymbol{u} \cdot \boldsymbol{f} = u_i f_i$ is preferentially positive near the particle surface and zero away from the particle where $f_i = 0$, resulting in $\Psi_p(t)$, the two-way coupling rate of change of TKE (3.5), being a positive quantity (figure 12). When $\boldsymbol{u} \cdot \boldsymbol{f}$ is positive, the particles impart a force, on the

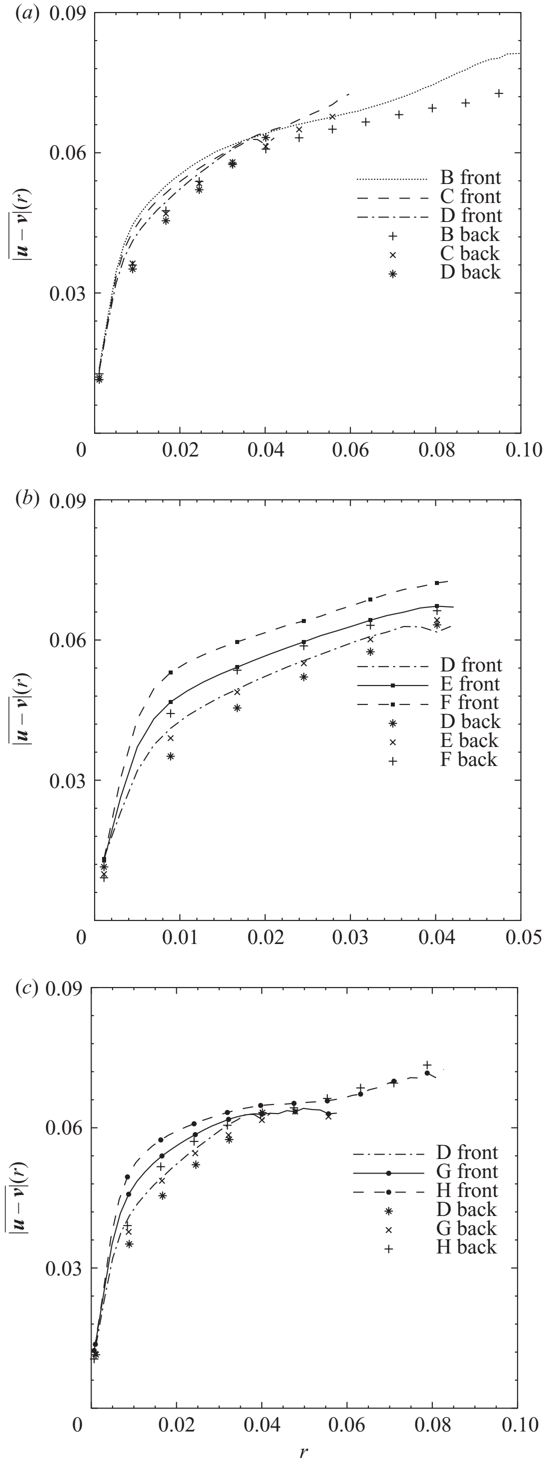

FIGURE 26. Fluid and particle velocity vector differences versus distance of the closest particle.

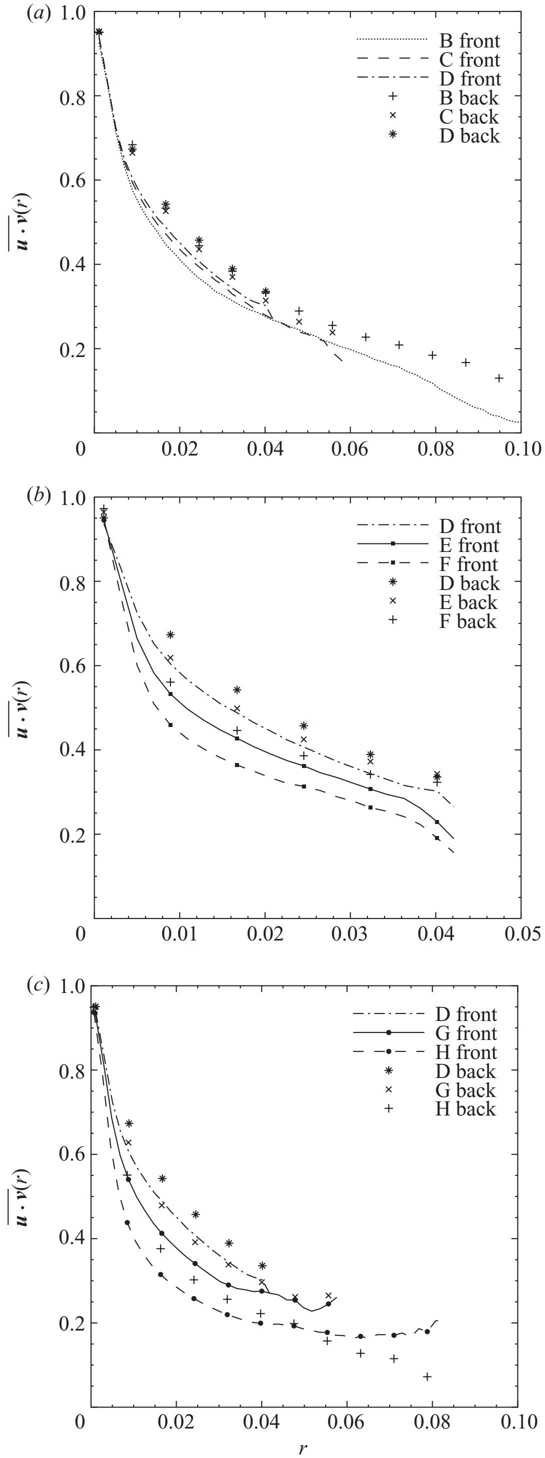

FIGURE 27. Fluid and particle velocity vector scalar products versus distance of the closest particle.

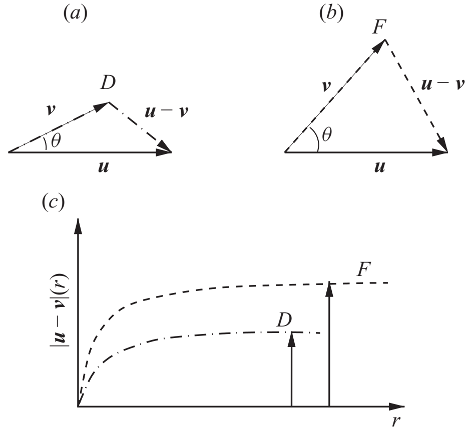

FIGURE 28. Schematic of the particle inertia effect on the difference between particle velocity and surrounding fluid velocity.

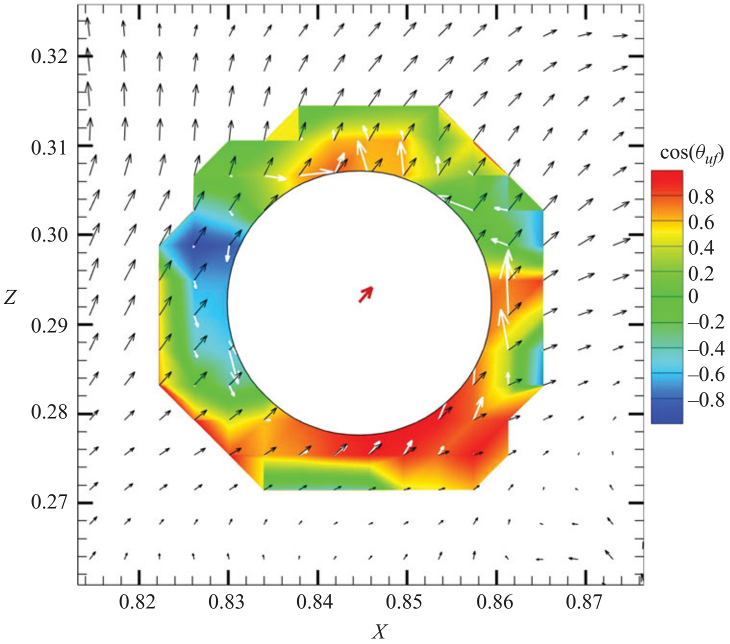

FIGURE 29. Two-dimensional instantaneous contours of $\cos\theta_{uf} = \boldsymbol{u}\cdot\boldsymbol{f}/|\boldsymbol{u}||\boldsymbol{f}|$ around a particle (case D). Fluid velocity vectors (black arrows), forcing vectors (white arrows) and particle velocity vector (red arrow).

surrounding fluid, in the same direction of the fluid velocity, resulting in a transfer of energy to the fluid and a positive $\Psi_p(t)$ (3.5).

Increasing the particle volume fraction (cases B–D) by increasing the number of particles (from 640 to 6400 with a fixed diameter) in the flow (table 3) increases the particle surface area affecting the surrounding fluid, thus increasing the two-way coupling force. Consequently, $\Psi_p(t)$ increases with volume fraction from case B to case D as shown in figure 12 (cases B–D). Increasing the particle-to-fluid density ratio for a fixed volume fraction and particle diameter (cases D–F) increases the forcing

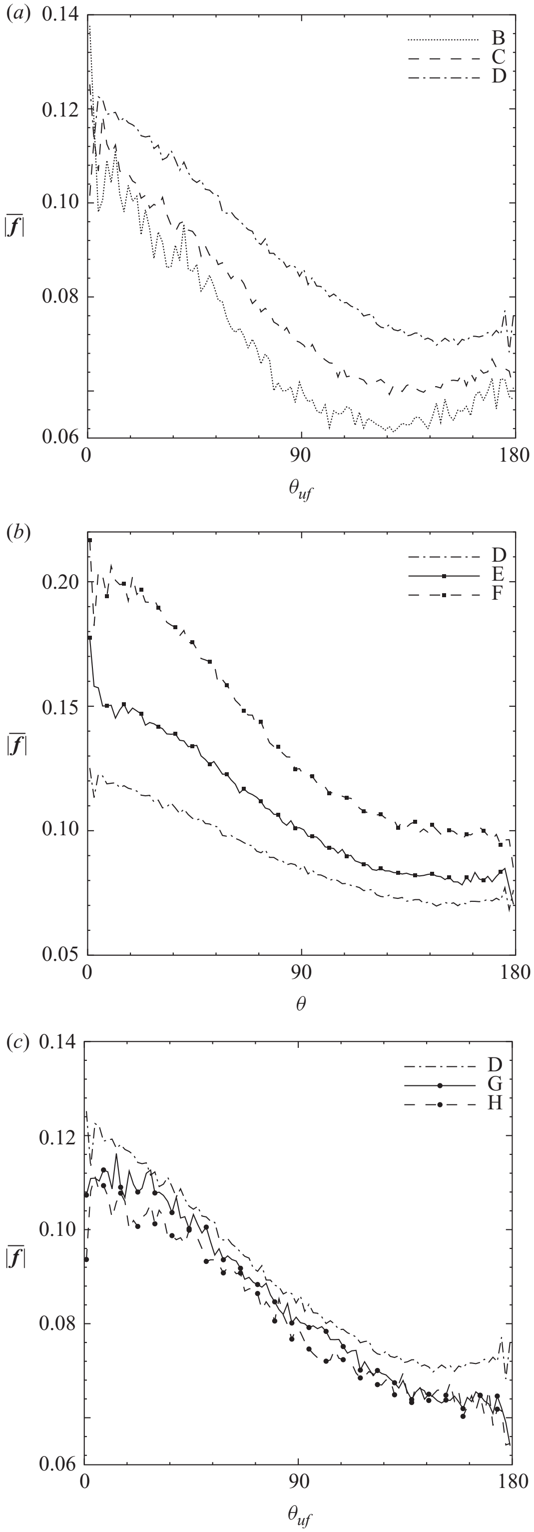

FIGURE 30. Ensemble-averaged magnitude of the two-way coupling force $\overline{|\boldsymbol{f}|}$ versus angle between $\boldsymbol{u}$ and $\boldsymbol{f}$, θ_{uf}.

on the surrounding fluid (figures 27, 31, 30 and table 6). The alignment of $\boldsymbol{u}$ and $\boldsymbol{f}$ increases with particle-to-fluid density ratio (table 6). Both the increase of $|\boldsymbol{f}|$ with particle density and the increased alignment of $\boldsymbol{u}$ and $\boldsymbol{f}$ result in an increase of $\Psi_p(t) = \langle u_i f_i \rangle$ from case D to E to F.

Increasing the particle diameter while fixing the volume fraction and mass fraction (cases D, G and H) increases the displacement of the surrounding fluid of each particle, thus increasing the magnitude of the two-way coupling force per particle, $\langle|\boldsymbol{f}|\rangle\,/particle$, ensemble averaged over the surrounding fluid (figure 31). However, increasing the particle diameter for a fixed volume fraction, ϕ_v, reduces the number of particles and total surface area. For example, doubling the particle diameter for a fixed ϕ_v reduces the number of particles by a factor of eight and reduces their total surface area by a factor of two. This reduction of the total contact area between the particles and the fluid reduces the two-way coupling force (figure 31). The net impact on $\Psi_p(t)$ of the above opposing effect (the increase of $\langle|\boldsymbol{f}|\rangle\,/particle$ and the reduction of the total number of particles) is that $\Psi_p(t)$ changes only slightly with increasing the particle diameter for a fixed ϕ_v as shown in figure 12 for cases D, G and H. Consequently, the observed changes in the decay rate of $E(t)$ for cases D, G and H (figure 9) are mostly due to the modifications of $\varepsilon(t)$ for these cases (figure 10), as discussed earlier, rather than due to the modifications of $\Psi_p(t)$.

3.3.3. *Effects of particle rotation*

Our results (figure 32) show that the effects of particle rotation on turbulence modulation are negligible in comparison to those of particle translation. Figure 32 shows the temporal development of $E(t)$ and its dissipation rate, $\varepsilon(t)$, for cases A, D (table 3) and I. In case I, not reported in table 3, the flow is laden with the same number and properties of the particles in case D, but in case I the particle rotation is set to zero, i.e. the particles in case I are only translating. At time $t = 2$, the percentage differences between the values of $E(t)$ and $\varepsilon(t)$ in cases D and I are only 1.7 % and 0.7 %, respectively.

Particles are released in the flow at $t = 1$ with zero angular velocity. The turbulent flow surrounding the particles creates asymmetric shear on the particle surface resulting in a non-zero angular momentum on the particles (the first term on the right-hand side of (2.20)). Increasing the volume fraction of particles with the same moment of inertia, by increasing their number (cases B–D), results in a faster decay of $E(t)$ (figure 9). This decay results in a reduction of both the magnitude of the shear rate at the particle surface and the angular momentum (the first term on the right-hand side of (2.20)). Consequently, the instantaneous ($t = 2$) ensemble-averaged angular velocity decreases (table 7).

Increasing the particle density while keeping the particle diameter constant (cases D–F) increases the moment of inertia (table 7) and reduces the angular momentum (the first term on the right-hand side of (2.20)) because $E(t)$ decays faster (figure 9), thus from (2.20) the angular velocity decreases (table 7).

Increasing the particle diameter (cases D, G and H), the moment of inertia increases as d^5 (table 7) while the angular momentum (the first term on the right-hand side of 2.20) increases as d^3, thus from (2.20) the angular velocity decreases (table 7).

3.3.4. *Turbulence energy spectrum*

Figure 33 shows the instantaneous three-dimensional energy spectra of the turbulence energy $E(k)$ at time $t = 5$ for cases A, D and E–H. Particles reduce

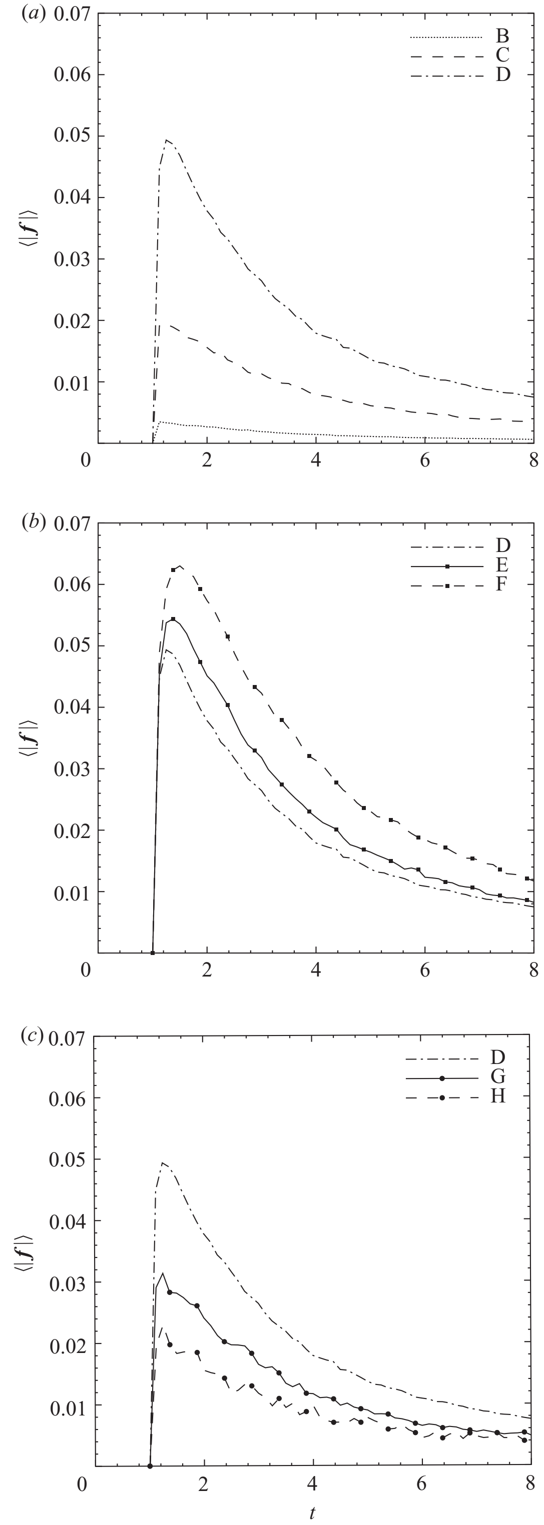

FIGURE 31. Temporal development of ensemble-averaged magnitude of the two-way coupling force, $\langle |\boldsymbol{f}| \rangle$.

Case	$I_p \times 10^9$	$\overline{\omega}_p$
B	3.84	0.87
C	3.84	0.84
D	3.84	0.83
E	7.50	0.63
F	15.0	0.48
G	19.7	0.64
H	181	0.39

TABLE 7. Particle moment of inertia, $I_p = (\pi/60)\rho_p d^5$, and instantaneous ensemble-averaged particle angular velocity, $\overline{\omega}_p$, at time $t = 2$.

$E(k)$ at small wavenumber compared to case A, e.g. for $1 \leqslant k < 32$ in cases D–F. This reduction is accompanied by an increase of $E(k)$ at larger wavenumbers (for $k > 32$ for cases D–F). However, the energy spectra $E(k)$ of the particle-laden cases show oscillations at $k > 32$ for cases D–F. These spectra are computed using the fluid velocity field at all the Eulerian mesh points in the computational domain including those points that are inside the particles at the time. This means that the fluid motion inside the particle contributes to the computed spectrum of TKE. The flow field inside the particle is the result of the correct numerical solution of the Navier–Stokes equations inside a hollow sphere. Of course, accounting for the fluid velocity inside the solid particles for computing $E(k)$ has no physical meaning. Moreover, setting the velocity inside the particle to zero only for computing $E(k)$ does not remove the oscillations. In order to understand the source of these oscillations, assume that the fluid velocity inside the particle is uniform. This uniform fluid velocity can be described by a ‘boxcar’ function (figure 34):

$$f(x) = \begin{cases} 1 & \text{for } |x| \leqslant d/2, \\ 0 & \text{for } |x| > d/2. \end{cases} \tag{3.6}$$

The Fourier transform of $f(x)$,

$$\mathscr{F}\{f(x)\} = F(\chi) = \frac{4}{\chi}\sin(\chi\, d/2), \tag{3.7}$$

is a $(\sin\chi)/\chi$ function of the wavenumber χ. In the discrete Fourier transform (DFT) domain, $\chi_k = 2\pi k/L$, where L is the length of the domain and k is the non-dimensional wavenumber normalized by the minimum $\chi_{k_{min}} = 2\pi/L$. Thus, the DFT of $f(x)$,

$$F(k) = \frac{L}{\pi k}\sin\left(\frac{\pi k d}{L}\right) \quad k = 1, \ldots, N/2, \tag{3.8}$$

whose spectrum is characterized by oscillations with a period L/d in the discrete k space (figure 35). For particle diameter $d = 0.031$ for cases B–F, $L/d = 32.2$, which is in agreement with the oscillations observed in figure 33, where the local minima of $E(k)$ are at $k = 32.2, 64.4$ and 96.4. Increasing the particle diameter reduces the period of the oscillations, L/d. In cases G and F, the period is $L/d = 23.2$ and 14.9, respectively, as observed in figure 33. This analysis proves that including the Eulerian velocity field inside the particles to compute the energy spectrum not only has no physical meaning but also corrupts the spectrum at all the wavenumbers.

We therefore used an alternative approach to avoid the corruption of wavenumber spectra by the presence of the particles in the three-dimensional Eulerian velocity field.

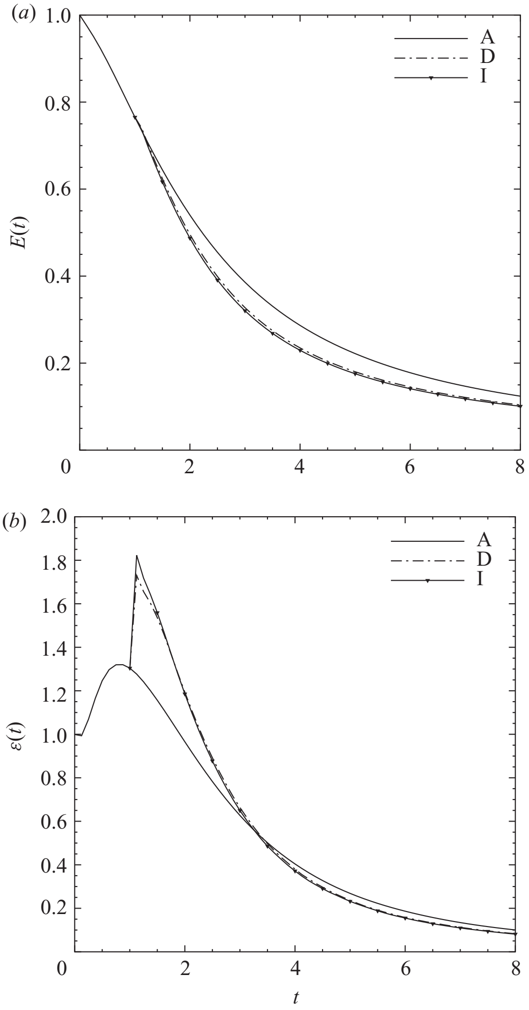

FIGURE 32. Temporal development of TKE, $E(t)$, and dissipation rate of TKE, $\varepsilon(t)$, in cases A, D and I.

Instead of a wavenumber spectrum, we compute the frequency spectrum of TKE using a Lagrangian approach. In addition to solving the Navier–Stokes equations (2.1) and (2.2) coupled with the particle equations of motion (2.19) and (2.20) to obtain the fluid velocity and track the particles, we compute the trajectories of 1.2×10^5 fluid points. These points are released at $t = 5$ randomly in the computational domain outside the spherical particles. The Lagrangian velocity of the fluid points is saved in time at intervals $\Delta_{fp} t = 8\Delta t$. In order to compute the frequency spectrum $E(\omega)$, we perform the cosine transform of the velocity autocorrelation

$$R_{ii}(\tau) = \langle u_i(t_0) u_i(t_0 + \tau) \rangle , \qquad (3.9)$$

$$E(\omega_n) = \frac{1}{N_t} \left[2 \sum_{j=1}^{N_t - 1} (R_{ii}(t_j) \cos(\omega_n t_j)) + R_{ii}(t_0) + (-1)^{N_t} R_{ii}(t_{N_t}) \right] , \qquad (3.10)$$

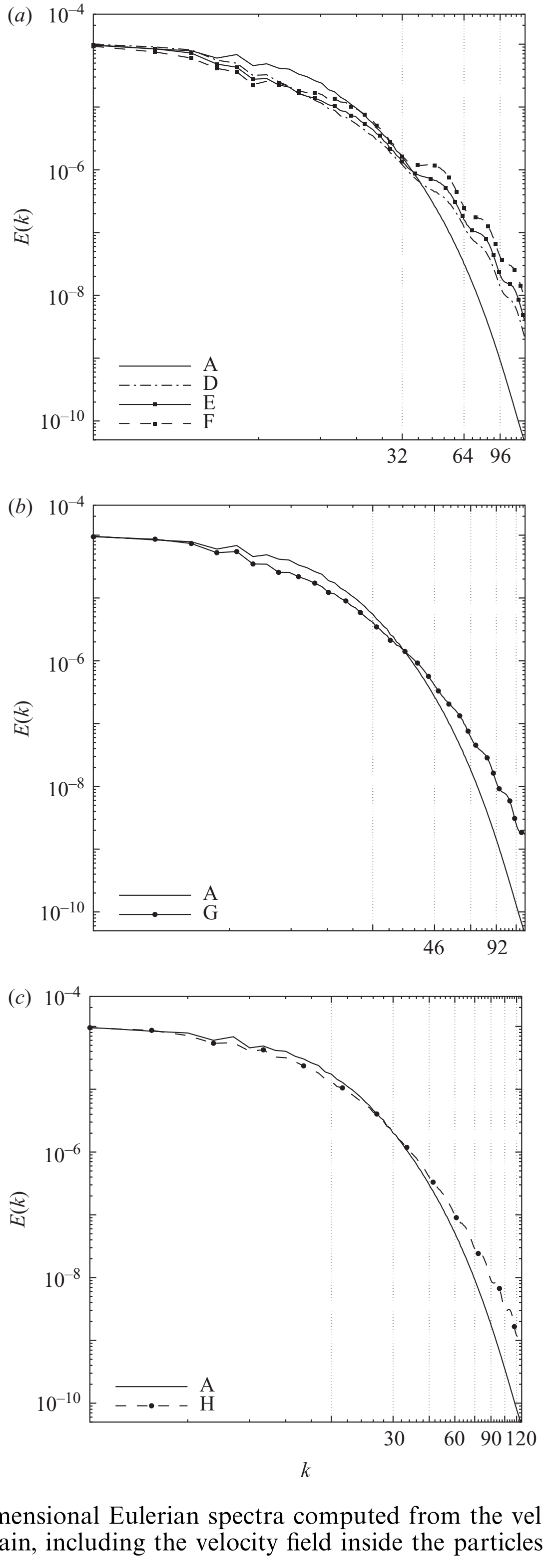

FIGURE 33. Three-dimensional Eulerian spectra computed from the velocity field throughout the domain, including the velocity field inside the particles at $t = 5$.

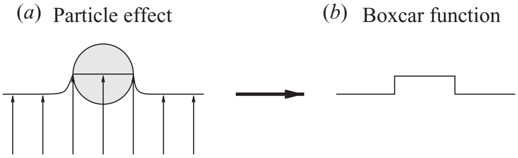

FIGURE 34. Schematic representing the similarity between the particle effect on the flow field and the 'boxcar' function.

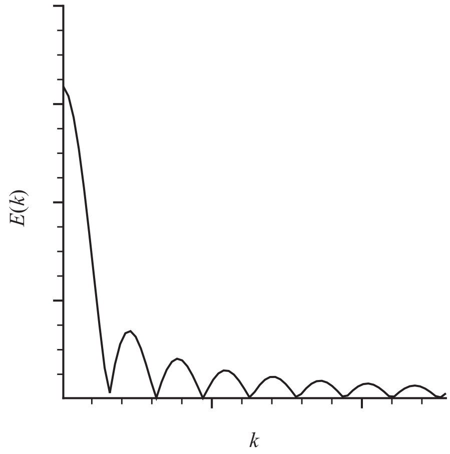

FIGURE 35. Spectrum of the 'boxcar' function showing the effect of the flow inside the particles on the Eulerian energy spectrum.

with frequency

$$\omega_n = \frac{\pi n}{N_t \Delta_{fp} t}, \tag{3.11}$$

where $n = 1, \ldots, N_t$, $t_j = j\Delta_{fp}t$, and N_t is the total number of time steps at which the Lagrangian velocity of the fluid points is saved. Note that (3.10) is strictly valid for statistically stationary turbulence. In order to limit the effect of the turbulence decay, we compute the energy spectrum in the time period from $t = 5$ to $t = 20$ during which Re_λ of the single-phase flow decreases from 32 to 25.

The Lagrangian frequency spectra are shown in figure 36 for all cases. The frequency ω is normalized by the Kolmogorov frequency $\omega_k = \pi/\tau_k$, where τ_k is the Kolmogorov time scale at $t_{inj} = 1$ (table 2). Particles reduce the frequency energy spectrum at low frequencies compared with that of single-phase flow (case A), i.e. particles decrease the energy of the large eddies of turbulence. Furthermore, figure 36 shows that particles (more pronounced in case F) increase the energy of the high frequencies, i.e. particles are increasing the energy of the small scales. This effect is more pronounced for heavier particles than that for lighter particles.

The modifications imparted to $E(\omega)$ by the particles are now explained. In finite-size particle-laden turbulence, the large eddy structures lose energy faster, i.e. get slower, than those in single-phase flow, because they are disrupted by the large-Stokes-number particles that drag the surrounding fluid in their direction (figure 27 and animation of TKE and ω_y). At the same time, particles generate, in their downstream direction, new eddies of size $d/2 \sim \lambda/2$ (ω_y contours in figure 25 and animation) that become more frequent in the flow, thus increasing the energy of the high frequencies (figure 36). In

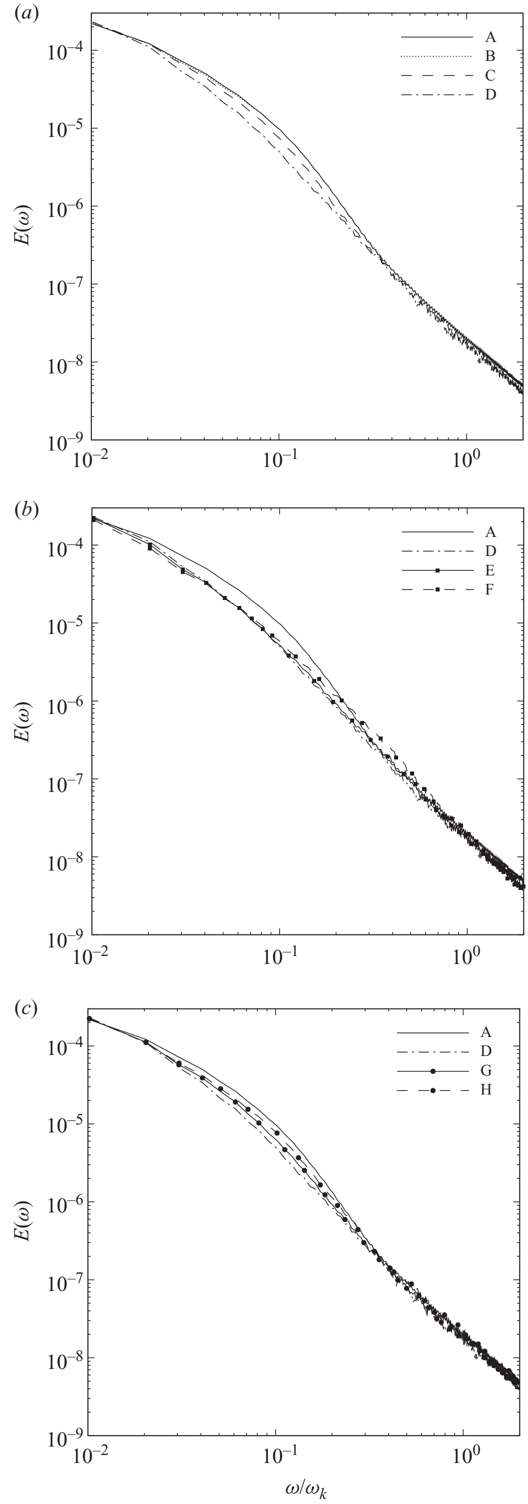

FIGURE 36. Energy frequency spectra computed with a Lagrangian method computed releasing the fluid points at $t = 5$.

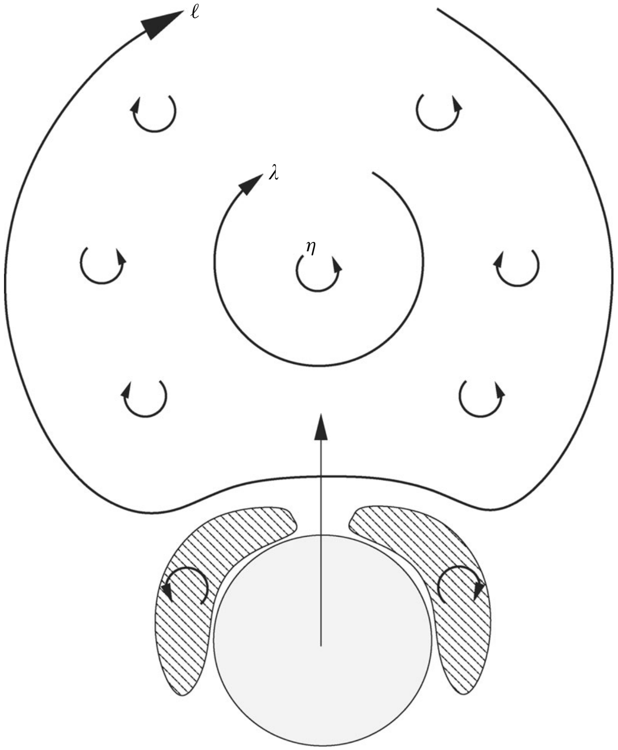

FIGURE 37. Sketch representing particle interacting with eddies of size integral length, ℓ, Taylor microscale, λ, and Kolmogorov length, η, for cases B–F.

summary, the particles break the 'order' of the large eddies which are less frequent and create new structures of size $d/2 \sim \lambda/2$, increasing the frequency of small eddies, thus decreasing the slope of the frequency spectrum (figure 36). This effect is sketched in figure 37.

4. Concluding remarks

This paper describes a DNS using the immersed boundary method to fully resolve all the relevant scales of turbulence around freely moving spherical particles of the Taylor length-scale size, $1.2 \leqslant d/\lambda \leqslant 2.6$, dispersed in a decaying isotropic turbulent flow. The notable advantages of the present immersed boundary method are the use of Cartesian mesh (in contrast to body-fitted mesh) and computational economy.

The particle diameter and Stokes number in terms of Kolmogorov length- and time scales are $16 \leqslant d/\eta \leqslant 35$ and $38 \leqslant \tau_p/\tau_k \leqslant 178$ at the time the particles are released in the flow. The particles mass fraction range is $0.026 \leqslant \phi_m \leqslant 1.0$, corresponding to a volume fraction of $0.01 \leqslant \phi_v \leqslant 0.1$ and density ratio of $2.56 \leqslant \rho_p/\rho_f \leqslant 10$. The maximum number of dispersed particles is 6400 for $\phi_v = 0.1$. The main results are as follows:

(*a*) Particles with diameter of the order of Taylor's length-scale always reduce the TKE, mostly by enhancing its dissipation rate, $\varepsilon(t)$. The augmented dissipation rate exceeds, $\Psi_p(t)$, the rate of increase of TKE due to the two-way coupling force imparted by the particles on the surrounding fluid (figure 14). The increased dissipation rate occurs close to the particle surface, mostly in its front, due to the increased strain rates (both extensional and compressive) as the particles move through the surrounding turbulent eddies (figures 16, 18, 20 and 21).

(*b*) For fixed volume fraction and diameter of the particles, the most pronounced effects on TKE, its dissipation rate and its rate of change due to two-way coupling occur by increasing the ratio ρ_p/ρ_f of particle to fluid densities (cases D–F ; figures 9, 10 and 12), which is directly proportional to the Stokes number, (τ_p/τ_k), and the particles mass fraction, ϕ_m.

(*c*) Increasing the particle diameter for fixed volume fraction and mass fraction (cases D, G and H) slightly reduces the dissipation rate of TKE (figure 10) because of the reduction of the number of particles and the corresponding total surface area responsible for inducing shear in the turbulent flow. However, the diameter increase has only a marginal effect on the two-way coupling rate of change of TKE (figure 12) due to two opposing effects: the increase of the *specific* two-way coupling force $(\langle|\boldsymbol{f}|\rangle\,/particle)$ and the reduction of the total number of particles. Thus, the larger the particle diameter for fixed ϕ_v and ϕ_m, the smaller the reduction of TKE relative to that of single-phase flow (figure 9).

(*d*) Particles with the same inertia, τ_p, and volume fraction but different diameters and density ratios (cases E and G) have different effects on TKE, $\varepsilon(t)$ and $\Psi_p(t)$ (figure 13). Smaller and heavier particles (case E) reduce TKE and increase both $\varepsilon(t)$ and $\Psi_p(t)$ more than the larger and lighter particles (case G). The larger reduction of TKE is due to the increase of $\varepsilon(t)$. The increase of $\varepsilon(t)$ from case G to E is due to the increase (44 %) of total surface area of the particles.

(*e*) Computing the spectrum $E(k)$ of turbulence energy including the velocity field inside the particles is unphysical and produces oscillations (figure 33) at wavenumbers proportional to L/d, where L is the side length of the computational cubic domain. In contrast, the frequency spectrum $E(\omega)$ (figure 36) is free from oscillations because it is computed using the Lagrangian velocity autocorrelations of a large number of fluid points in the flow surrounding the particles.

(*f*) Comparing the present results with those of our earlier DNS for particles with $d/\eta < 1$ and $\tau_p/\tau_k \sim 1$ (Ferrante & Elghobashi 2003), we observe the following:
(i) For particles with $d < \eta$, both $E(t)$ and $\varepsilon(t)$ may be larger than those of the single-phase flow for $\tau_p/\tau_k < 0.25$, or smaller for $\tau_p/\tau_k > 0.25$. In contrast, for particles with $d > \eta$, as in the present study, $E(t)$ is always smaller than that of the single-phase flow, case A, while $\varepsilon(t)$ is always larger than that of case A after the release of the particles in the flow and then decreases at later times relative to that of case A.
(ii) The two-way coupling rate of change of TKE, ψ_p, can be positive or negative for particles with $d < \eta$, while it is always positive for particles with $d > \eta$.

Appendix. Equations of conservation of linear and angular momenta for a solid particle moving in an incompressible fluid

In order to derive the equations of conservation of linear and angular momenta for a solid spherical particle which is simulated with the immersed-boundary method, we start with Newton's second law for the linear and angular motions of a rigid body:

$$\rho_p V_p^{(m)} \dot{\boldsymbol{u}}_p = \iint_{\mathscr{S}} \boldsymbol{\tau} \cdot \boldsymbol{n} \; \mathrm{d}\mathscr{S} + \rho_p V_p^{(m)} \boldsymbol{g}, \tag{A 1}$$

$$I_p \, \dot{\boldsymbol{\omega}}_p = \iint_{\mathscr{S}} \boldsymbol{r} \times (\boldsymbol{\tau} \cdot \boldsymbol{n}) \; \mathrm{d}\mathscr{S}, \tag{A 2}$$

where ρ_p, V_p and I_p are the density, volume and moment of inertia of the particle; $\boldsymbol{u}_p$ and $\boldsymbol{\omega}_p$ are the linear and angular velocities of the particle; $\dot{\boldsymbol{u}}_p = \mathrm{d}\boldsymbol{u}_p/\mathrm{d}t$ and

$\dot{\boldsymbol{\omega}}_p = \mathrm{d}\boldsymbol{\omega}_p/\mathrm{d}t$ are the linear and angular accelerations of the particle; $\boldsymbol{\tau} = -\boldsymbol{I}p + \mu(\nabla\boldsymbol{u} + \nabla\boldsymbol{u}^{\mathrm{T}})$ is the stress tensor; $\boldsymbol{n}$ is the unit vector pointing outward normal to the particle surface $\mathscr{S}$; $\boldsymbol{r} = \boldsymbol{x} - \boldsymbol{x}_p$ is the position vector of the particle surface, $\boldsymbol{x}$, relative to the particle centre, $\boldsymbol{x}_p$; and $\boldsymbol{g}$ is the gravitational acceleration.

In order to evaluate the first term on the right-hand sides of (A 1) and (A 2), we invoke the principle of conservation of linear and angular momenta, i.e. the rate of change of linear (angular) momentum of a volume of fluid $\mathscr{V}$ equals the sum of total internal and external forces exerted on $\mathscr{V}$ (Aris 1962, p. 100):

$$\frac{\mathrm{d}}{\mathrm{d}t}\iiint_{\mathscr{V}} \rho_f \boldsymbol{u}\,\mathrm{d}\mathscr{V} = \iint_{\mathscr{S}} \boldsymbol{\tau}\cdot\boldsymbol{n}\,\mathrm{d}\mathscr{S} + \iiint_{\mathscr{V}} \rho_f \boldsymbol{f}\,\mathrm{d}\mathscr{V} + \iiint_{\mathscr{V}} \rho_f \boldsymbol{g}\,\mathrm{d}\mathscr{V}, \tag{A 3}$$

$$\frac{\mathrm{d}}{\mathrm{d}t}\iiint_{\mathscr{V}} \rho_f (\boldsymbol{r}\times\boldsymbol{u})\,\mathrm{d}\mathscr{V} = \iint_{\mathscr{S}} \boldsymbol{r}\times(\boldsymbol{\tau}\cdot\boldsymbol{n})\,\mathrm{d}\mathscr{S} + \iiint_{\mathscr{V}} \rho_f (\boldsymbol{r}\times\boldsymbol{f})\,\mathrm{d}\mathscr{V}, \tag{A 4}$$

where ρ_f is the fluid density, and $\boldsymbol{f}$ and $\boldsymbol{g}$ (gravity) are the external forces per unit mass exerted on the volume $\mathscr{V}$. In the case of a solid particle immersed in a fluid, $\boldsymbol{f}$ is the force per unit mass exerted by the particle on the fluid. For a sphere that satisfies the rigid-body motion immersed in an incompressible fluid, Uhlmann (2003) has shown that

$$\frac{\mathrm{d}}{\mathrm{d}t}\iiint_{\mathscr{V}} \boldsymbol{u}\,\mathrm{d}\mathscr{V} = V_p \dot{\boldsymbol{u}}_p, \tag{A 5}$$

independently from the actual $\boldsymbol{u}$ inside the volume $\mathscr{V}$. An analogous simplification for the left-hand side of (A 4) holds in the case of rigid-body motion throughout the volume $\mathscr{V}$:

$$\boldsymbol{u}(\boldsymbol{x}) = \boldsymbol{u}_p + \boldsymbol{\omega}_p \times \boldsymbol{r}(\boldsymbol{x}), \quad \boldsymbol{x}\in V \Rightarrow \frac{\mathrm{d}}{\mathrm{d}t}\iiint_{\mathscr{V}} (\boldsymbol{r}\times\boldsymbol{u})\,\mathrm{d}\mathscr{V} = \frac{I_p}{\rho_p}\dot{\boldsymbol{\omega}}_p. \tag{A 6}$$

However, in this study the Lagrangian points are distributed only at the particle surface, and the interior of the particle is not forced to be in rigid-body motion, thus (A 6) does not hold, and the left-hand side of (A 4) (the last term in (A 14)) is computed numerically.

Using (A 3)–(A 5), Newton's second law (A 1) and (A 2) can be written as

$$(\rho_p - \rho_f) V_p \dot{\boldsymbol{u}}_p = -\rho_f \iiint_{\mathscr{V}} \boldsymbol{f}\,\mathrm{d}\mathscr{V} + (\rho_p - \rho_f) V_p \boldsymbol{g}, \tag{A 7}$$

$$I_p \dot{\boldsymbol{\omega}}_p = -\rho_f \iiint_{\mathscr{V}} (\boldsymbol{r}\times\boldsymbol{f})\,\mathrm{d}\mathscr{V} + \frac{\mathrm{d}}{\mathrm{d}t}\iiint_{\mathscr{V}} \rho_f (\boldsymbol{r}\times\boldsymbol{u})\,\mathrm{d}\mathscr{V}. \tag{A 8}$$

The volume integral of the first term on the right-hand side of (A 7) and (A 8) can be computed as follows. Using the properties of the delta function (2.12)–(2.13), δ_h, adopted in the immersed-boundary method (§ 2.2.1), it can be shown that the total amount of forces (and torques) imparted at the Eulerian grid points surrounding the particle equals the sum of forces (and torques) at the Lagrangian points distributed over the sphere surface (Uhlmann 2005):

$$\sum_{\boldsymbol{x}\in\mathscr{D}} \boldsymbol{f}(\boldsymbol{x}) h^3 = \sum_{m=1}^{N_p}\sum_{l=1}^{N_L} \boldsymbol{F}\left(\boldsymbol{X}_l^{(m)}\right)\, \Delta V_l^{(m)}, \tag{A 9}$$

$$\sum_{\boldsymbol{x}\in\mathscr{D}} \boldsymbol{x}\times\boldsymbol{f}(\boldsymbol{x}) h^3 = \sum_{m=1}^{N_p}\sum_{l=1}^{N_L} \boldsymbol{X}_l^{(m)} \times \boldsymbol{F}\left(\boldsymbol{X}_l^{(m)}\right)\, \Delta V_l^{(m)}. \tag{A 10}$$

The integrals over the particle volume V in (A 1) and (A 2) can be written as

$$\iiint_{\mathscr{V}} \boldsymbol{f}\,\mathrm{d}\mathscr{V} = \sum_{\boldsymbol{X}\in\mathscr{V}} \boldsymbol{f}(\boldsymbol{x})h^3 = \sum_{l=1}^{N_L} \boldsymbol{F}\big(\boldsymbol{X}_l^{(m)}\big)\ \Delta V_l^{(m)}, \tag{A 11}$$

$$\iiint_{\mathscr{V}} (\boldsymbol{r}\times\boldsymbol{f})\,\mathrm{d}V = \sum_{\boldsymbol{X}\in\mathscr{V}} \boldsymbol{r}\times\boldsymbol{f}(\boldsymbol{x})h^3 = \sum_{l=1}^{N_L} \big(\boldsymbol{X}_l^{(m)} - \boldsymbol{x}_p^{(m)}\big)\times\boldsymbol{F}\big(\boldsymbol{X}_l^{(m)}\big)\ \Delta V_l^{(m)}. \tag{A 12}$$

Substituting (A 11) and (A 12) in (A 7) and (A 8) gives the linear and angular momenta equations for the mth particle

$$\big(\rho_p^{(m)} - \rho_f\big)V_p^{(m)}\dot{\boldsymbol{u}}_p^{(m)} = -\rho_f\sum_{l=1}^{N_L}\boldsymbol{F}\big(\boldsymbol{X}_l^{(m)}\big)\Delta V_l^{(m)} + \big(\rho_p^{(m)} - \rho_f\big)V_p^{(m)}\boldsymbol{g}, \tag{A 13}$$

$$\begin{aligned} I_p^{(m)}\dot{\boldsymbol{\omega}}_p^{(m)} = {} & -\rho_f\sum_{l=1}^{N_L}\left(\boldsymbol{X}_l^{(m)} - \boldsymbol{x}_p^{(m)}\right)\times\boldsymbol{F}(\boldsymbol{X}_l^{(m)})\Delta V_l^{(m)} \\ & + \rho_f\frac{\mathrm{d}}{\mathrm{d}t}\iiint_{\mathscr{V}^{(m)}}\big[\big(\boldsymbol{x} - \boldsymbol{x}_p^{(m)}\big)\times\boldsymbol{u}\big]\,\mathrm{d}\boldsymbol{x}. \end{aligned} \tag{A 14}$$

We acknowledge the support of NSF TeraGrid for computing time on IBM-BlueGeneL at San Diego Supercomputer centre.

Supplementary movies are available at journals.cambridge.org/flm.

REFERENCES

Aris, R. 1962 *Vectors, Tensors and the Basic Equations of Fluid Dynamics*. Dover.

Brown, D., Cortez, R. & Minion, M. 2001 Accurate projection methods for the incompressible Navier–Stokes equations. *J. Comput. Physics* **168** (2), 464–499.

Eggels, J. G. M. & Somers, J. A. 1995 Numerical simulation of free convective flow using the lattice-Boltzmann scheme. *Intl J. Heat Fluid Flow* **16**, 357–364.

Elghobashi, S. & Truesdell, G. C. 1992 Direct simulation of particle dispersion in a decaying isotropic turbulence. *J. Fluid Mech.* **242**, 655–700.

Elghobashi, S. & Truesdell, G. C. 1993 On the two way interaction between homogeneous turbulence and dispersed solid particles. I. Turbulence modifications. *Phys. Fluids* A **5** (7), 1790–1800.

Ferrante, A. 2004 Reduction of skin-friction in a microbubble-laden spatially developing turbulent boundary layer over a flat plate. PhD thesis, University of California, Irvine.

Ferrante, A. & Elghobashi, S. 2003 On the physical mechanism of two-way coupling in particle-laden isotropic turbulence. *Phys. Fluids* **15** (2), 315–329.

Ferrante, A. & Elghobashi, S. 2007 On the effects of finite-size particles on decaying isotropic turbulence. *International Conference on Multiphase Flow*. Leipzig.

Glowinski, R., Pan, T., Hesla, T., Joseph, D. & Périaux, J. 2001 A fictitious domain approach to the direct numerical simulation of incompressible viscous flow past moving rigid bodies: application to particulate flow. *J. Comput. Phys.* **169**, 363–426.

Lu, J., Fernandez, A. & Tryggvason, G. 2005 The effect of bubbles on the wall drag in a turbulent channel flow. *Phys. Fluids* **17**, 095102-1-12.

Lumley, J. L. 1978 Two-phase and non-newtonian flows. *Topics Phys.* **12**, 290–324.

Maxey, M. R. & Riley, J. 1983 Equation of motion for a small rigid sphere in a turbulent fluid flow. *Phys. Fluids* **26** (4), 883–889.

Mordant, N. & Pinton, J. 2000 Velocity measurement of a settling sphere. *Eur. Phys. J.* B. *Condensed Matter Complex Systems* **18** (2), 343–352.

PESKIN, C. 1972 Flow patterns around heart valves: a digital computer method for solving the equations of motion. PhD thesis, Albert Einstein College of Medicine.

PESKIN, C. 2002 The immersed boundary method. *Acta Numer.* **11**, 1–39.

ROMA, A., PESKIN, C. & BERGER, M. 1999 An adaptive version of the immersed boundary method. *J. Comput. Phys.* **153**, 509–534.

ROSALES, C. & MENEVEAU, C. 2005 Linear forcing in numerical simulations of isotropic turbulence: physical space implementations and convergence properties. *Phys. Fluids* **17**, 095106-1-8.

SAFF, E. B. & KUIJLAARS, A. B. J. 1997 Distributing many points on a sphere. *Math. Intell.* **19** (1), 5–11.

SCHUMANN, U. 1977 Realizability of Reynolds-stress turbulence models. *Phys. Fluids* **20**, 721.

SNYDER, W. H. & LUMLEY, J. L. 1971 Some measurements of particle velocity autocorrelation functions in a turbulent flow. *J. Fluid Mech.* **48**, 41.

TEN CATE, A., DERKSEN, J. J., PORTELA, L. M. & VAN DEN AKKER, H. E. A. 2004 Fully resolved simulations of colliding monodisperse spheres in forced isotropic turbulence. *J. Fluid Mech.* **519**, 233–271.

UHLMANN, M. 2003 First experiments with the simulation of particulate flows. *Tech. Rep.* 1020. CIEMAT, Madrid, Spain.

UHLMANN, M. 2005 An immersed boundary method with direct forcing for the simulation of particulate flows. *J. Comput. Phys.* **209**, 448–476.

UHLMANN, M. 2008 Interface-resolved direct numerical simulation of vertical particulate channel flow in the turbulent regime. *Phys. Fluids* **20**, 053305.

ZHANG, Z. & PROSPERETTI, A. 2005 A second-order method for three-dimensional particle simulation. *J. Comput. Phys.* **210**, 292–324.